The Pattern of Temporal Redox Shifts Can Determine If Anaerobic Fe^{II} or CH_4 Production Dominates

*Diego Barcellos, Ashley Campbell, Jennifer Pett-Ridge, and Aaron Thompson**

Corresponding Author:

Aaron Thompson: Department of Crop and Soil Sciences, University of Georgia. Athens, GA 30605, USA Email: AaronT@uga.edu

Authors:

Diego Barcellos: Department of Environmental Sciences, Federal University of São Paulo (UNIFESP), Diadema, São Paulo, Brazil. 09913.

Ashley Campbell: Lawrence Livermore National Laboratory. Livermore, CA 94550, USA.

Life & Environmental Sciences Department, University of California Merced, Merced, CA 95343, USA

Jennifer Pett-Ridge: Lawrence Livermore National Laboratory. Livermore, CA 94550, USA.

Aaron Thompson: Department of Crop and Soil Sciences, University of Georgia. Athens, GA 30605, USA

KEYWORDS: upland soils; iron biogeochemistry; redox oscillations; soil carbon; methane emissions.

ABSTRACT: Temporal redox fluctuations alter the pools of reducible Fe^{III} and greenhouse gas emissions in humid upland soils. However, it is less clear how the characteristics of these fluctuations (length, frequency, amplitude) impact biogeochemical rates. We hypothesized that anaerobic rates of Fe^{III} reduction and CH_4 emissions are sensitive to the length of soil oxygen deprivation. To test this hypothesis, we exposed a surface soil from the Luquillo Experimental Forest to three lengths of O_2 perturbation during repeated redox oscillations: an anoxic interval of 6 d with oxic intervals of 8, 24, or 72 h. We found that shorter oxic intervals resulted in more anaerobic Fe^{III} reduction, while longer oxic intervals stimulated higher anaerobic CH_4 emissions (CO_2 fluxes did not change). We propose that short O_2 pulses stimulate Fe reduction by resupplying the Fe^{III} electron acceptor, but do not last long enough to inhibit microbial Fe reducers; conversely long O_2 pulses suppress microbial iron reducers to a greater extent than methanogens leading to enhanced CH_4 emissions. Thus, the length of periodic oxidant exposure selectively enhances less thermodynamically favorable anaerobic processes by modulating the competitiveness of dominate anaerobic bacteria, which is important for regulating greenhouse gas emissions in redox dynamic soils.

Short synopsis statement: In redox-dynamic soils, the length of O_2 exposure (oxic period) can determine which anaerobic processes proliferate during anoxic periods.

Introduction

Redox variability is ever present in soils [1, 2] and drives critical biogeochemical processes for several elements and molecules (iron, manganese, methane, nitrate, and others) [3-6]. This is most evident in the spatial redox heterogeneity that emerges within microsites and along flow paths and can yield vastly different redox conditions separated by a cm or less in soils [7, 8]. Oxygen depletion commonly manifests within aggregates and other soil features that restrict the water flow and hence the replenishment of O_2 necessary to support carbon decomposition [9, 10]. Mottling, concretions, and liesegang bands are common visual expressions of spatial redox heterogeneity [11-13]. But temporal redox variability is also common and emerges within individual microsites or in bulk soil pores due to shifting water content, carbon availability, and oxygen depletion [14-16]. While spatial redox heterogeneity manifests as distinct redox-static biogeochemical niches, temporal redox heterogeneity forces direct competition between microbial groups and thus generates niches where soil taxa must tolerate redox conditions that are dynamic [17-19]. Pett-Ridge, et al. [20] and Pett-Ridge, et al. [21] showed that specific microbial communities maintain adaptation to shifting redox conditions and, in some locations, have adapted to specific redox fluctuation periodicity, i.e., a fluctuation every 4 days. Altering the periodicity in these soils, shifted the microbial community [22].

Currently, redox variability is represented in global biogeochemical models as discrete processes turned on or off based on soil moisture [3, 23, 24]. In this manner, rates of CH_4 or CO_2

production (for instance) are scaled to the time under anoxic or oxic conditions [15, 25, 26]. This is a valid approach only if redox status is a state variable, such that the pattern of redox changes does not matter, only whether the system was oxic or anoxic. However, redox fluctuation patterns do matter, at least for some processes and for some fluctuation parameters. Three redox fluctuation parameters can reasonably define the *pattern* of redox fluctuations: periodicity (the recurrence rate of low redox events), amplitude (the rates of O_2 introduction or consumption), and duration (the length any low or high redox condition persists; Fig. S1) [14, 26-28].

Prior exposure to anoxic conditions is known to impact anaerobic biogeochemical processes by conditioning indigenous anaerobic communities [29-31]. But, if the period of time between anoxic events is too long anaerobic communities lose this conditioning or are replaced by aerobes; conversely too short an anoxic event and certain anoxic processes (e.g., methane generation) may never develop [32, 33]. Most anaerobic processes also depend on electron acceptors that can be renewed by a pulse of O_2 (e.g., Fe^{III}, Mn^{IV}, NO_3, SO_4, etc.), although the kinetics of oxidation varies [34-36]. Furthermore, periodic oxic conditions increase the nominal oxidation state of carbon (NOSC), which can increase the concentration of organic matter electron donors that are more thermodynamically favorable for anaerobic processes [37, 38].

Thus, periodicity or re-introduction of O_2 is clearly important, even while biogeochemical processes may be insensitive to changes in periodicity except at the extremes of very short fluctuations or the difference between a fluctuating system and an essentially permanently oxic or anoxic system [8, 15, 23]. For instance, while redox fluctuations generally increase Fe reduction rates relative to non-redox fluctuating systems [27, 28], variations in the periodicity do not appear to impact these rates unless the frequency becomes very rapid [14]. In the case of Fe reduction, re-oxidation of Fe^{2+} generates fresh electron-accepting Fe^{III} phases that are preferentially reduced

over bulk Fe^{III} (i.e., rapidly reducible Fe^{III}, Fe^{III}_{RR}), with faster oxidation rates (amplitude) producing more rapidly-reducible Fe^{III} minerals than slower oxidation events [26]. If the availability of electron acceptors is limiting, then maximum Fe reduction rates should occur at short redox oscillation frequencies—as Calabrese, Barcellos, Thompson and Porporato [23] has shown in a theoretical paper predicting maximal Fe reduction rates as a function of the redox dynamics using the frequency and mean depth of rainfall events [39]. However, this does not account for the timescales of microbial growth and activation, which undoubtably constrain biogeochemical processes in redox dynamic systems. In many humid upland soils, redox conditions oscillate on timescales that are shorter than organisms can respond via population growth (typically 4 days or longer) [15]. Under these conditions, constitutive enzymes, metabolic plasticity, and physiological tolerance mechanisms ("breath holding") may all be important strategies [40, 41]. At the landscape scale, this would allow O_2 respiring taxa to coexist with fermenters and a wide variety of anaerobes/ facultative taxa that use terminal electron acceptors other than O_2.

We expect the integrated biogeochemical responses to dynamic redox conditions will depend considerably on how various processes and their abiotic and biotic drivers are alternately constrained or enhanced. Since very short redox fluctuations should stimulate Fe reduction [14, 23], we sought to evaluate the role of oxic exposure length on Fe reduction and competing anaerobic processes. Here we focus on the production of CH_4, which can occur through a combination of fermentation and anaerobic microbial respiration [42], and may be suppressed when Fe reducers outcompete methanogens for acetate and hydrogen substrates [31, 43]. Conversely, methanotrophs can participate in Fe^{III} oxide reduction via CH_4 oxidation under anoxic conditions [29, 44, 45]—this may be an important sink for CH_4 in soils [46]. We hypothesized that during redox fluctuations,

soils exposed to brief oxic intervals (τ_{oxic}) would exhibit higher Fe reduction rates during subsequent anoxic intervals (τ_{anoxic}) than those exposed to longer oxic intervals, and that these higher Fe reduction rates would suppress CH_4 emissions. We tested this by exposing a redox fluctuating soil to variable lengths of oxic exposure (maintaining similar lengths of anoxia) while monitoring Fe^{II} concentrations, CO_2 and CH_4 efflux, Fe mineral composition, and soil microbial community composition.

Methods

Site and sample characterization

Five soil cores were collected from 0-10 cm depth in a valley location at the Bisley Research Watershed in the Luquillo Experimental Forest (LEF), Puerto Rico (Luquillo Critical Zone Observatory, LCZO). The sampleswere placed in plastic bags, stored in a cooler at ambient temperature, and immediately shipped to the University of Georgia within 24 h of sampling. The field-moist samples were then carefully homogenized and sieved (2-mm) under anoxic conditions in a 95%:5% (N_2:H_2) glovebox[47] (Fig. S2). Initial soil moisture content of the fresh soil was 77 %. Soils from the Bisley watershed are predominantly Ultisols (Typic Haplohumults) formed from volcanic parent material, weakly acidic, and mineralogically composed of quartz, kaolinite, chlorite, and goethite [48]. The soil redox oscillates on timescales of several days [17]. Total Fe and Al content were determined by ICP-MS following a Li-metaborate fusion. Standard short-range-ordered (SRO) Fe and Al phases were obtained by citrate/ascorbate extraction (0.2 M sodium citrate/0.05 M ascorbic acid), and analyzed by ICP-MS. The native soil (prior to incubation) contained 943 ± 4 and 439 ± 7 mmol kg^{-1} soil of total-Fe and SRO-Fe^{III}, respectively (Table S1).

128

Redox oscillations and iron reduction

130 We subjected natural soils to suspensions (1:10 soil:solution ratio) to three different redox oscillation treatments for up to 47 days. Soil slurries (suspensions) were constantly mixed on an 132 orbital shaker (250 rpm) to decrease soil heterogeneity and force microbial interactions; essentially magnifying the competition that might occur within a single microsite [8]. Our 134 experimental design was similar to that described in Barcellos, Cyle and Thompson [14], but with fresh, field-moist soils instead of air-dried soils (to better capture ambient microbial community 136 dynamics). The soil slurries were buffered with a solution to maintain the natural soil pH (5.5) with MES (2-N-morpholino-ethanesulfonic acid) with KCl as a background electrolyte. Each 138 treatment contained triplicate reactors, which contained 4.5 g (dry-weight equivalent) of soil in a 2 mM KCl + 10 mM MES buffered solution at pH 5.5 ± 0.2, with a 45 g final suspension mass. 140 Soil slurries were placed in a 95%:5%:0% (N_2:H_2:O_2) glovebox (Coy anaerobic chamber) for the anoxic condition and were exposed to laboratory room air (~21% O_2) for the oxic condition, both 142 constantly shaking on an orbital shaker at 250 rpm and in the dark. Ferrous iron (Fe^{II}) was measured every 8 to 72 h by withdrawing 0.5 mL of suspension from the same vessel using wide 144 orifice pipette tips (to avoid soil particle size exclusion and keeping the same soil:solution ratio), adding 0.5 M HCl, shaking for 2 h, centrifuging at 11,000 RCF (relative centrifugal force) for 10 146 min, and taking the supernatant for analysis [47, 49]. Concentrations of Fe^{II} after ferrozine colorimetric analysis were obtained from 562 nm (and 500 nm) in a spectrophotometer [50].

148 In parallel reactors, dissolved O_2 (DO) was monitored through a single redox oscillation cycle (undergoing oxic and anoxic conditions) in triplicate reactors using a Hach (USA) DO meter. 150 Within 1 h after exposing anoxic soil slurries to oxic conditions, DO increased to > 7.0 mg L^{-1}

(>84.7 %). Likewise, for soil slurries that were previously exposed to oxic conditions over 24 hours, we observed that DO decrease from 9.90 to 0.24 mg L^{-1} (~100 to 2.4 %) within 2 h and reached 0.06 mg L^{-1} (0.73%) after 24 h of anoxia (Table S2).

We aimed to test the influence of O_2 exposure on Fe reduction rates and implications on CO_2 and CH_4 emissions by changing the time soils would be exposed to oxygen (τ_{oxic}) from 72, 24, and 8 h coupled with a long anoxic period (τ_{anoxic}) of 144 h (6 d) (Table 1). We started our experiment by pre-conditioning all reactors to three sequential oscillation periods of 6-d anoxic and 1-d oxic, in order to acclimate the soil's microbial communities to repetitive identical shifts in redox conditions. Thus, after the pre-conditioning period (at 480 h), we split the reactors into three treatments, undergoing three consecutive redox cycles as follows: Ox-72 with 144 h anoxic + 72 h oxic, Ox-24 with 144 h anoxic + 24 h oxic, and Ox-8 with 144 h anoxic + 8 h oxic (Table 1). Control treatments with either constant anoxic or oxic conditions were also included (n=3).

Trace gases and carbon analyses

Fluxes of CO_2 (in mmol kg^{-1} of soil h^{-1}) and CH_4 (in μmol kg^{-1} of soil h^{-1}) were measured at approximately the beginning, middle, and end of each redox cycle. For each gas flux measurement, we capped the triplicate reactors with rubber septa and sampled the headspace gas at 0, 10, and 30 minutes with gastight syringes and stored in pre-evacuated 3 mL glass vials. Samples were analyzed in a gas chromatograph (Shimadzu GC-14A, Japan) using a flame ionization detector (FID) and electron capture detector (ECD). Nitrogen (280 kPa) was used as the carrier gas and the flow in the column was 24.3 mL min^{-1}. Measurements of CO_2 and CH_4 were used to calculate both instantaneous fluxes (in mmol kg^{-1} of soil h^{-1} and μmol kg^{-1} of soil h^{-}

$^{-1}$, respectively) and cumulative fluxes (in mmol kg^{-1} of soil and μmol kg^{-1} of soil, respectively)—
174 calculated by multiplying the instantaneous flux by all hours prior to the measurement.

Samples for total carbon and nitrogen were analyzed via combustion in a CHN Carlo Erba
176 Elemental Analyzer. The native soil (no treatment added) had 37.4 mg g^{-1} of total C and 2.2 mg g^{-1} of total N (solid phase). The MES buffer added another 7.5 mg of C, comprising 14% of
178 carbon in each reactor, which made for 44.9 mg g^{-1} of total C at the start of the experiment. Dissolved organic carbon (DOC) from the aqueous phase (supernatant after centrifugation) of the
180 soil slurry at the end of redox oscillation for each treatment was measured in a Shimadzu 5050 TOC.

182

Mössbauer spectroscopy

184 Detailed Fe speciation was determined by Mössbauer Spectroscopy at the temperatures 50 K, 35 K, 25 K, 13 K, 5 K. We collected triplicate soil samples at the end of the last (third) oxic
186 interval for the treatments Ox-72, Ox-24, Ox-8, and for the common soil used in all treatments at the beginning of the experiment (initial soil). We pooled together the triplicate oxic samples to
188 form one soil sample, placed those samples in a ring that was covered with Kapton tape to avoid gas diffusion, and immediately froze the sample in a −20 °C freezer. The samples were placed in
190 our Mössbauer spectrometer's cryostat (pre-cooled to below 140 K), operating with a He atmosphere to prevent the oxidation of any Fe^{II} by oxygen. The Mössbauer spectra were recorded
192 in transmission mode with He cooled cryostat containing variable-temperature (Janis Research Co.) and a channel detector (1024). Detailed information for the Mössbauer spectra modeling
194 and fitting parameters (Figures S3 to S6 and Tables S3 to S6) are provided in the Supplementary Material.

196

Microbial analyses

198 Duplicate samples were collected at the beginning of the experiment, at the end of the last τ_{oxic}, and at the end of the last τ_{anoxic} for all treatments (Ox-72, Ox-24, and Ox-8). From each sample, 200 we extracted microbial DNA from 0.25 g of soil using an in-house phenol-chloroform extraction described in the supplemental materials [51-53]. The extracted DNA was submitted for 16S rRNA 202 gene sequencing. The 16S rRNA amplicons were generated using custom barcoded 515f-806r primers. All samples were multiplexed and paired end sequencing (2x250) was performed on the 204 MiSeq (Illumina). Other details regarding the microbial analyses are provided in Section 2 of the Supplemental Material.

206

Analyses of Metabolites (acetate) by NMR

208 We collected the aqueous phase from the reactors (supernatant after centrifugation) at the end of the last (third) oxic interval for the treatments Ox-72, Ox-24, Ox-8, and Pre-Conditioning, 210 to perform metabolite analyses (acetate) by Nuclear magnetic resonance spectroscopy (NMR). Details for the analyses are provided in Section 3 of the Supplemental Material.

212

Statistical analyses

214 To compare the effect of the different redox oscillation treatments on Fe^{II} concentrations and cumulative CO_2 and CH_4 fluxes, we performed ANOVA analysis using a Kenward-Roger 216 approximation and parametric bootstrap function for linear mixed models, using the lmer function from the lme4 package in R [54, 55]. To correlate the effect of preceding τ_{oxic} on 218 anaerobiosis of Fe and C, we computed linear regressions individually for each of the treatments

comparing two of these variables at a time (Fe^{II} and CH_4), under anoxic conditions only, using lm function from the lme4 package in R. We further conducted a one-way ANOVA to test for differences in acetate concentrations among the treatments, for the soil samples collected in the last (third) oxic interval.

Results and Discussion

Ferrous iron dynamics and iron reduction rates

We cycled all treatments through three pre-conditioning redox cycles (6 d reduction followed by 24 h of oxidation; Table 1) to verify that all replicates were behaving similarly and exhibiting significant increases in Fe^{II} during the anoxic intervals and sharp drops in Fe^{II} during the oxic periods (Fig. 1); this pre-conditioning also removed any "start-up" effects of the experiment. After the pre-conditioning cycles, we split the treatments for an additional three redox cycles so that three replicates each had either an 8 h, 24 h or 72 h exposure to O_2 followed by again a similar 6 d of anoxia (Table 1; Fig. 1 and S7). All replicates continued to behave as expected, with Fe^{II} increasing during anoxic periods, followed by sharp drops when O_2 was reintroduced [14, 19]; Fe reduction rates and peak Fe^{II} concentrations remained similar ($p > 0.05$) *within* a given treatment from the first to the third experimental redox cycle.

We found anoxic Fe^{II} production differed depending on the length of Oxic exposure. Incubations with the shortest O_2 exposure (Ox-8 treatment) had both greater Fe^{II} concentrations (Fig. 2a) and higher Fe reduction rates (0.26 ± 0.05 mmol kg^{-1} h^{-1}; Fig. 3a) relative to the Ox-24 and Ox-72 treatments (Fig. 2a). Fe reduction rates in the pre-conditioning period and the Ox-24 treatment (which had identical τ_{oxic} and τ_{anoxic}) were very similar (0.16 ± 0.03 mmol kg^{-1} h^{-1}),

while rates in the Ox-72 soils were slightly lower (0.12 ± 0.02 mmol kg^{-1} h^{-1}), but the difference was not significant (Fig. 3a).

Shorter O_2 perturbations stimulated faster Fe reduction rates

Short pulses of O_2 (shorter τ_{oxic}) in an otherwise anoxic system evidently stimulate faster anoxic Fe reduction rates than longer O_2 exposures. We discuss potential explanations for this by considering in turn the factors governing soil Fe reduction rates, principally: the availability of Fe^{III} electron acceptors, the availability of labile carbon substrates (electron donors), and the activities of microbial Fe reducers [17, 40, 56, 57]. Higher Fe reduction rates following shorter O_2 exposure time could be explained by a greater abundance of electron acceptors, more available electron donors, and/or a more active Fe reducer population in those treatments.

To assess differences in the availability of Fe^{III} electron acceptors, we analyzed solid phase samples by Mössbauer spectroscopy at the end of the last (third) oxic interval for the contrasting treatments Ox-8 and Ox-72. Mössbauer spectroscopy is highly sensitive to the crystallinity of Fe oxide phases when run across a temperature gradient, with less crystalline phases—which are typically more available for Fe^{III} reduction—requiring a lower collection temperature to magnetically order into a Mössbauer sextet [6]. We found the Mössbauer sextet abundance was similar for both the Ox-8 and Ox-72 samples at 50K, 35K and 5K, with slightly higher sextet abundance in the Ox-8 samples (46.4 ± 1.1 % and 51.6 ± 1.0 %) than the Ox-72 (41.7 ± 2.4 % and 46.9 ± 2.4 %) samples at 25K and 13K, respectively (Figures 4, and S3 to S6; Tables S3 to S6). This could be interpreted as the Ox-8 samples had higher crystallinity (and thus less availability for Fe reduction) than the Ox-72 samples. However, the Ox-8 sextets at 25K and 13K are more skewed toward lower hyperfine field strengths (Bhf 47.5 and 47.9, respectively)

than the Ox-72 sextets (Bhf 47.9 and 48.4, respectively), which suggests the portions of Fe phases in the Ox-8 samples that order at 25K and 13K—while more abundant than the in Ox-72 samples—are comparatively less crystalline. In all cases, these differences are minor and much less pronounced than changes in both treatments relative to the initial soil (Figures S3 to S6 and Tables S3 to S6), or changes reported previously in response to redox fluctuations [50]. This suggests no significant differences in SRO-mineral crystallinity exist following the oxidation events. Furthermore, while it is well understood that pO_2 (as well as Fe^{II} oxidation rates[6, 26, 58]) impacts the formation and crystallinity of incipient Fe^{III}-minerals all of our treatments were exposed to similar pO_2 (~21% O_2). The length of O_2 exposure (8 h to 72 h) could feasibly generate different amounts of crystal ripening as some find in laboratory syntheses at high temperature [59] and under acidic conditions [60], but our Mössbauer data suggests this does not happen in our experiment.

We also tested for differences in labile organic matter (electron donors) by measuring water extractable dissolved organic matter content (DOC) present at the beginning of the final anoxic interval. Total DOC (corrected for the abundance of MES organic buffer) was statistically similar ($p>0.05$) for the Ox-72 and Ox-8 soils (155 ± 13 and 170 ± 21 mg L^{-1} respectively). We also used nuclear magnetic resonance spectroscopy (NMR) to evaluate the volatile fatty acids (VFAs) in the samples and found acetate concentrations were not statistically different ($p>0.05$) between the pre-condition, Ox-8, Ox-24, and Ox-72 treatments (Fig. S8). Further, CO_2 emissions were similar throughout the experiment across the Ox-72, Ox-24, and Ox-8 treatments (Fig. S9). Consequently, we surmise that the supply of labile organic substrates for Fe reducers did not differ with the different O_2 pulse lengths in our experiment.

We also tested whether differences in microbial community composition (particularly Fe reducers) could underpin the differences we observed in Fe^{II} production rates. The metabolism of Fe reducers is generally thought to be inhibited during oxic conditions, due to both competition for reductants with aerobic organisms (which use O_2 as an electron acceptor, a far more thermodynamically favorable reaction [61]) and because O_2 is toxic to many anaerobic organisms and can trigger anaerobes to generate protective enzymes or form cysts [62]. It is possible that very short pulses of O_2 (i.e., < 0.5 h) in an otherwise anoxic environment may not be sufficient for aerobic organisms to out-compete Fe-reducers for reduced-C electron donors, whereas very long exposure to O_2 (i.e., 2 weeks) cause more sweeping changes in microbial community composition and growth-efficiency.

In our study, while the length of exposure to oxic conditions did change microbial community-composition between treatments (Fig. 5c), we found no statistical difference in the relative abundance or overall composition of iron-reducers at the end of the Ox-8, Ox-24, and Ox-72 treatments (Fig. 5a). Dominant iron reducing genera in our soils included *Anaeromyxobacter, Bacillus, Desulfitobacterium, Desulfobulbus, Desulfosporosinus, Desulfovibrio, Geobacter, Geothrix,* and *Klebsiella* (Fig. 5a). *Anaeromyxobacter* and *Geobacter* have been previously detected in similar soils exposed to slow and fast oxidation rates [28], and are frequently observed in poorly-drained/depressional soils [63]. *Geobacter* sp. can tolerate O_2 exposure over 24 h [64], but little is known regarding their competitive advantage for short O_2 exposures, since their temporal threshold for O_2 tolerance is unknown. If the threshold for Fe-reducers to maintain activity is between 8 h and 24 h for our system, this could explain the higher Fe reduction rates we observed in the treatments with shorter τ_{oxic}. The ability of Fe reducers to rapidly resume activity

after O_2 exposure or shifts in the availability of reducible Fe^{III} phases could explain the increased anaerobic Fe reduction rates we observed with decreasing oxygen exposure time.

The implications of an Fe redox cycle that is modulated by O_2 exposure length could be profound. The principal intersection of the Fe redox cycle with ecosystem function is via its coupling with the C cycle [6, 34, 65, 66], and Fe is a critical elemental sorbent for, as an example, the key plant nutrient phosphorus [48, 67, 68]. Incorporating the dynamics of these Fe cycle roles into global ecosystem models has been challenging because it has not been clear how to tie changes soil moisture to Fe reduction rates [7, 69, 70]. In a first step forward, Calabrese, Barcellos, Thompson and Porporato [23] has shown that the theoretical maximum in cumulative ecosystem Fe reduction will occur when redox fluctuations are as frequent as possible given the growth and activity constraints of microbial Fe reducers. Our results further this theory and we postulate that microbial Fe reducers likely thrive in environments with short pulses of O_2, which should be predictable based on rainfall patterns [17, 69, 71]. Some studies estimate as much as 50% of the C mineralization in humid soils could be coupled to Fe reduction [14]—an estimate supported by the theoretical work of Calabrese, Barcellos, Thompson and Porporato [23]—and other work [6] suggests an acceleration of the Fe reduction cycle would likely lead to a net decrease in organic matter persistence through destabilization of mineral associated organic matter (MAOM). Further, P behavior can become dominated by Fe cycle dynamics in redox dynamic systems [67] as the oxidation of Fe^{II} generates SRO Fe^{III} phases that sorb phosphorus, which are then subsequently dissolved during reduction events [68, 72, 73].

Longer O_2 perturbations lead to higher CH_4 emissions

In contrast to our Fe reduction results, anaerobic CH_4 emissions increased when we lengthened the O_2 exposure intervals (Figs. 2 and 3). While the general pattern of instantaneous CH_4 flux was similar across treatments (i.e., increasing CH_4 flux over the 6-d anoxic period followed by a sharp decrease during oxic periods), CH_4 fluxes were more pronounced in the Ox-72 and Ox-24 treatments than in the Ox-8 treatments (Fig. 2b). Cumulative CH_4 fluxes decreased significantly with decreasing oxic exposure length (Ox-72 > Ox-24 > Ox-8), with the Ox-24 treatment maintaining similar CH_4 fluxes to the pre-conditioning cycles (which had 24-h oxic periods) (Fig. 3b and S). Thus, lengthening the oxic exposure to 72 hrs increased CH_4 fluxes, while decreasing oxic exposure to 8 hrs decreased CH_4 fluxes.

Fe^{III} reduction is well known to suppress methane production in soils, as Fe reducers can outcompete methanogens for acetate or H_2 [31, 74]. This is likely why within each anoxic interval, we do not see CH_4 emissions begin to increase until Fe reduction rates begin to decline (Fig. 2 and 3). Higher Fe reduction rates in the shorter τ_{oxic} treatments could thus be expected to suppress methane emissions more than in longer τ_{oxic} treatments (Fig. 2 and 3). To examine this, we plotted rates of Fe^{II} and CH_4 for each treatment and found the Fe^{II}:CH_4 production regression slope shifts from 0.29 to 1.32 for the Ox-72 to Ox-8 treatments (Fig. S11, Table S7), consistent with greater anaerobic Fe^{II} production and lower anaerobic CH_4 fluxes following shorter O_2 exposure (Fig. S12, Table S7). The generation of rapidly reducible SRO Fe^{III} phases during each oxidation event undoubtably fuels Fe reducer activity. As others have separately shown, experimental additions of SRO Fe^{III} to similar Luquillo Experimental Forest (LEF) soils can stimulate iron-reducers to outcompete methanogens [31]. What is less clear is why longer oxic exposure length appears to diminish Fe^{II} production more than CH_4 emissions.

Anaerobe tolerance to O_2

The ability of anaerobic organisms to tolerate periodic exposure to molecular oxygen is essential for them to survive and thrive in redox fluctuating environments and we have shown previously that organisms populating the LEF soils are adapted to frequent redox shifts [20, 28, 40]. In our current experiment, it appears that longer O_2 exposure has a negative effect on the activity of Fe reducers, but that methanogens are not similarly constrained. In fact, in the Ox-72 treatment, where Fe reduction rates were the lowest, CH_4 fluxes begin to increase immediately upon the initiation of the τ_{anoxic} interval, whereas in the Ox-24 and Ox-8 treatment, CH_4 fluxes were typically delayed for ~48 h (Fig. 2). As was the case for Fe reducers, we observed no significant differences in the relative abundance of methanogens across the treatments (Fig 5b), but this does not preclude differences in activity[75]. The dominant methanogen was *Methanobacterium sp.* (Fig. 5b), which can recovery rapidly following O_2 exposure [76, 77]. Indeed, although methanogens are strict anaerobes, recent findings suggest they are less affected by O_2 exposure than often appreciated [30, 76-78], with some species producing CH_4 even when cultured with low levels of O_2 (up to 1%) [79]. While it is understood that longer O_2 exposure can lower subsequent anaerobic activity for methanogen cultures [80], recovery times can be as short as 1-day [76] and full viability can often be preserved after week to month long exposures to O_2 [81], especially when low-redox microsites or other anaerobic microbes are present [31, 76, 82]. More complex interactions between iron and methane might also explain the suppression of CH_4 fluxes during periods of high Fe reduction, such as the coupling of anaerobic oxidation of methane to Fe reduction by methanotrophic archaea and bacteria [83, 84] or direct interspecies electron transfer (DIET) processes [85, 86], which link Fe reducers, methanotrophs, and methanogens [87].

Environmental Implications

Our findings illustrate that the duration of oxygen exposure is a particularly important determinant of Fe reduction rates—a fundamental ecosystem process in upland soils. Short periods of oxygen exposure are likely to drive rapid Fe reduction, whereas longer oxic exposure might hinder Fe reduction. Likely as a consequence of this control on Fe reduction, we found that the amount of time redox-dynamic soils are exposed to oxygen can affect the balanced of iron reduction and methane emissions in the subsequent anoxic interval. For soils exposed to 6 d of anoxia, as oxygen exposure decreases from 72 to 24 to 8 hours, the subsequent anaerobic intervals have higher Fe reduction rates and lower CH_4 emissions, with no change in CO_2 fluxes.

The influence of variable redox conditions on an ecosystem manifest through the timescales and rates of the governing processes [88]. For instance, a key consequence of a shift from oxic to anoxic conditions is the solubilization of phosphorus [68, 89, 90], organic matter [10, 19, 91], and various contaminant metals [92-94] associated with the reductive dissolution of high surface area Fe oxides that often sorb these constituents [95]. But, the release of these constituents is governed by the kinetics of Fe reduction, which can be sluggish or extremely rapid depending on environmental conditions. Frequent redox fluctuations have been shown previously[14] and theoretically[23] to favor high Fe reduction rates, and here we now show that specifically *the length of O_2* exposure modulates Fe reduction rates. Soil ecosystems that favor short periods of oxygenation of soil microsites, should also favor faster Fe reduction rates, and greater releases of sorbed constituents.

Our study probed the biogeochemical dynamics of a single microsite by forcing microbial competition in a slurried soil reactor. Stimulating Fe reduction has long been shown to curtail methane production in wetlands and soil systems. With spatial heterogeneity minimized, our

work here suggests methanogens will be less affected by longer O_2 exposure than Fe reducers, and thus might have a competitive advantage in systems become oxygenated for long periods of time, such as through extensive soil drainage or drying. Conversely, we might expect frequent, short aeration events to minimize to methane production in systems with appreciable Fe redox cycling.

Supporting Information

The Supporting Information contains four sections comprising twelve additional figures, seven additional tables, and three additional method descriptions.

Funding Sources

Funding for this research was provided by National Science Foundation (NSF), grants EAR-1331841 and DEB-1457761.

ACKNOWLEDGMENTS

We thank all members of Aaron Thompson's Lab (especially Nehru Mantripragada and Kim Kauffman) and members of Jennifer Pett-Ridge's lab for technical assistance, as well as our NSF Luquillo Critical Zone Observatories (LCZO) collaborators. Work at Lawrence Livermore National Laboratory was performed under the auspices of U.S. Department of Energy Contract DE-AC52- 07NA27344 and Office of Science Genomic Sciences award SCW1478. Thanks to

Daniel Markewitz, Lori Sutter, and Aaron Joslin for support with GC analyses. Thanks to FAPESP (São Paulo State Research Foundation), grant 2019/02855-0. Thanks to the researchers at Environmental Molecular Sciences Laboratory (EMSL) of the Pacific Northwest National Laboratory (PNNL) David Hoyt, Elizabeth Eder, Allison Wong, and Rosalie Chu for performing metabolite analysis in the NMR. Part of this research (NMR analysis) was performed using EMSL (grid.436923.9), a DOE Office of Science User Facility sponsored by the Office of Biological and Environmental Research.

Author Contributions

Diego Barcellos: Conceived and designed the experiments; Performed the experiments; Analyzed the data; Contributed materials/analysis tools; Wrote the paper.

Ashley Campbell: Analyzed the data; Contributed materials/analysis tools; Wrote the paper.

Jennifer Pett-Ridge: Conceived and designed the experiments; Analyzed the data; Contributed materials/analysis tools; Wrote the paper.

Aaron Thompson: Conceived and designed the experiments; Analyzed the data; Contributed materials/analysis tools; Wrote the paper.

Declaration of competing interest:

The authors declare no conflicts of interest.

TABLE AND FIGURES

440

442 **Table 1.** Treatments for different oscillation periods and τ_{oxic} or τ_{anoxic} durations in hours (and days).

444

446

Treatment	τ_{oxic}	τ_{anoxic}	$\tau_{oxic}/\tau_{anoxic}$ ratio	Num. of Cycles
Pre-conditioning (15 vessels)	24 h	144 h (6 d)	1:6	3

Started different treatments | *At 480 h of experiment*

Treatments	τ_{oxic}	τ_{anoxic}	$\tau_{oxic}/\tau_{anoxic}$ ratio	Reps	Num. of Cycles
Ox-72h	72 h (3 d)	144 h (6 d)	1:2	3	3
Ox-24h	24 h	144 h (6 d)	1:6	3	3
Ox-8h	8 h	144 h (6 d)	1:18	3	3

+ Anoxic Control (3 reps)

+ Oxic Control (3 reps)

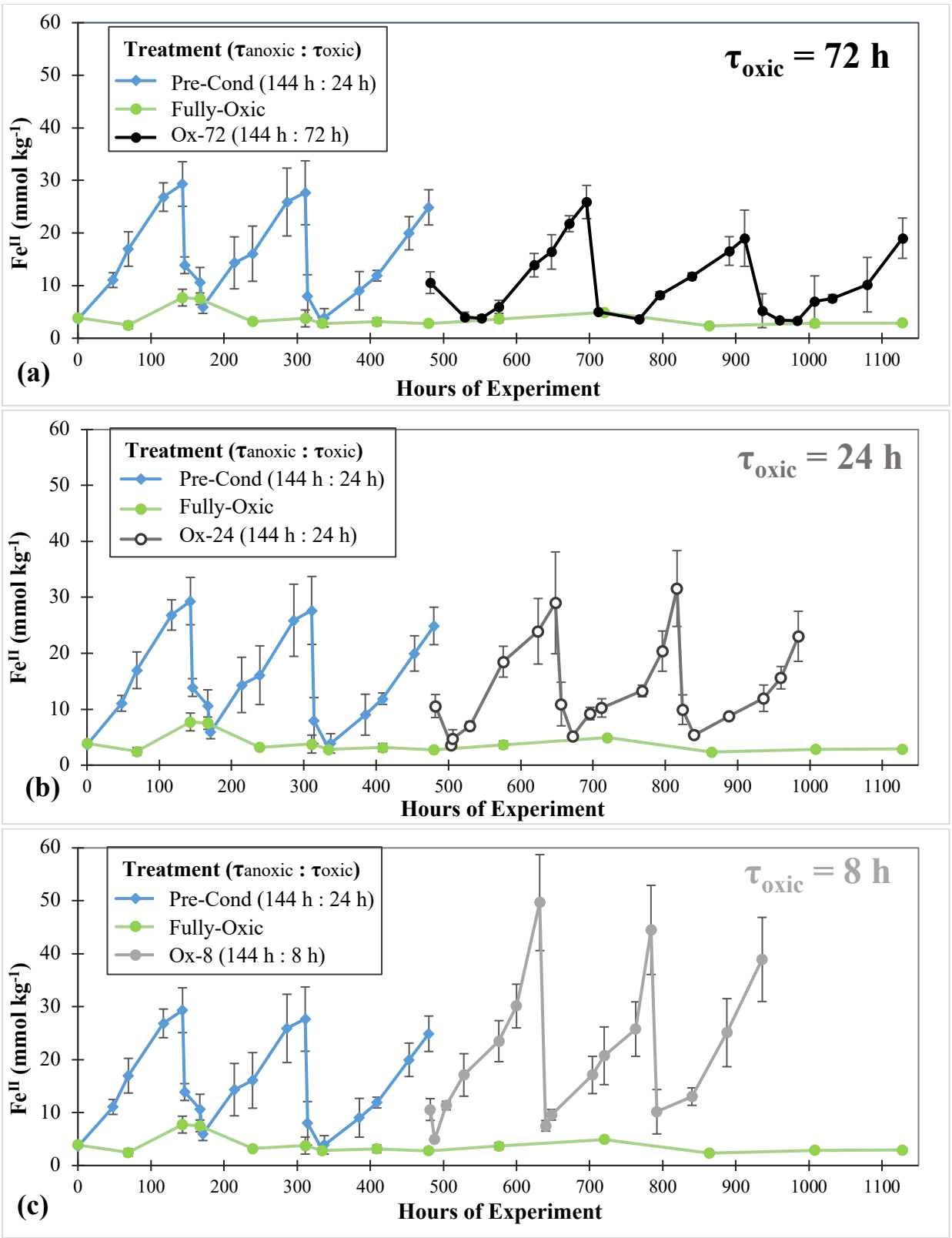

Figure 1. Soil Fe^{II} dynamics (mean ± 1 standard deviation) for soils incubated with multiple headspace redox treatments, including a pre-conditioning period (τ_{oxic} = 24 h), a fully oxic

treatment, and three treatments with decreasing τ_{oxic} of 72, 24, and 8 h (a, b, and c, respectively). In the oxic control treatment (non-fluctuating), Fe^{II} concentrations remained steady (3.8 ± 0.5 mmol kg^{-1}) throughout the experiment. See anoxic control in Fig. S7.

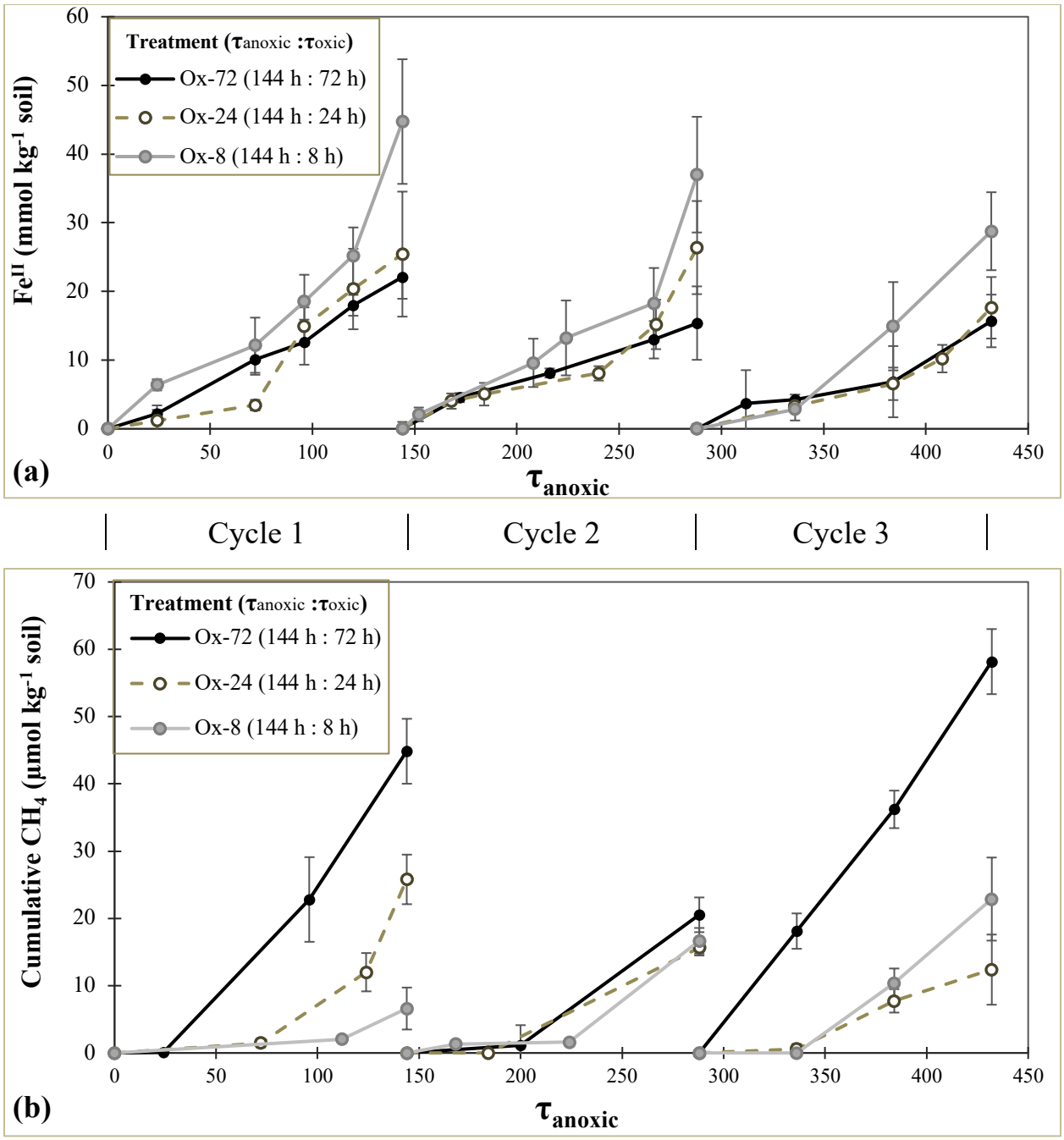

458

460 **Figure 2.** (a) Fe^{II} concentrations normalized to initial concentration at each cycle (mean ± 1 standard deviation) over anoxic conditions (τ_{anoxic}) only, for the treatments with decreasing τ_{oxic} of 462 72, 24, and 8 h; (b) Cumulative CH_4 normalized to initial concentration at each cycle (mean ± 1 standard deviation) over anoxic conditions (τ_{anoxic}) only, for the treatments with decreasing τ_{oxic} of 464 72, 24, and 8 h.

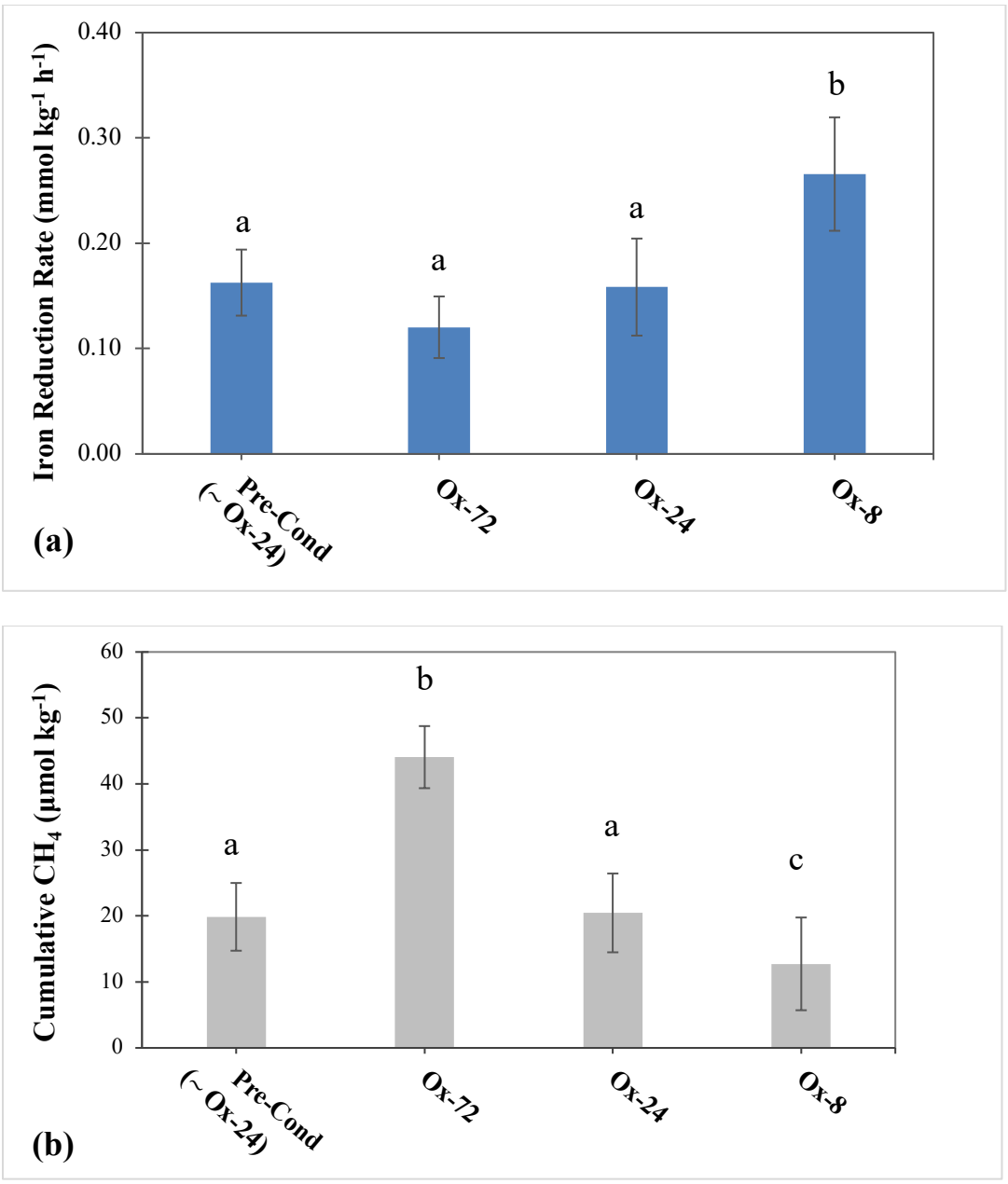

Figure 3. (a) Averaged Fe reduction rates with n=3 redox cycles for the pre-conditioning and treatments with τ_{oxic} of 72, 24, and 8 h. (b) Cumulative CH_4 during τ_{anoxic} for each treatment. Lowercase letters in parentheses (a and b) indicate significant differences at the 5% probability level. The error bars indicate a ± 1 standard deviation. Summary of results: Alterations in Fe^{II} and CH_4 during anoxic conditions (τ_{anoxic}), with changes in the preceding τ_{oxic} for the different treatments.

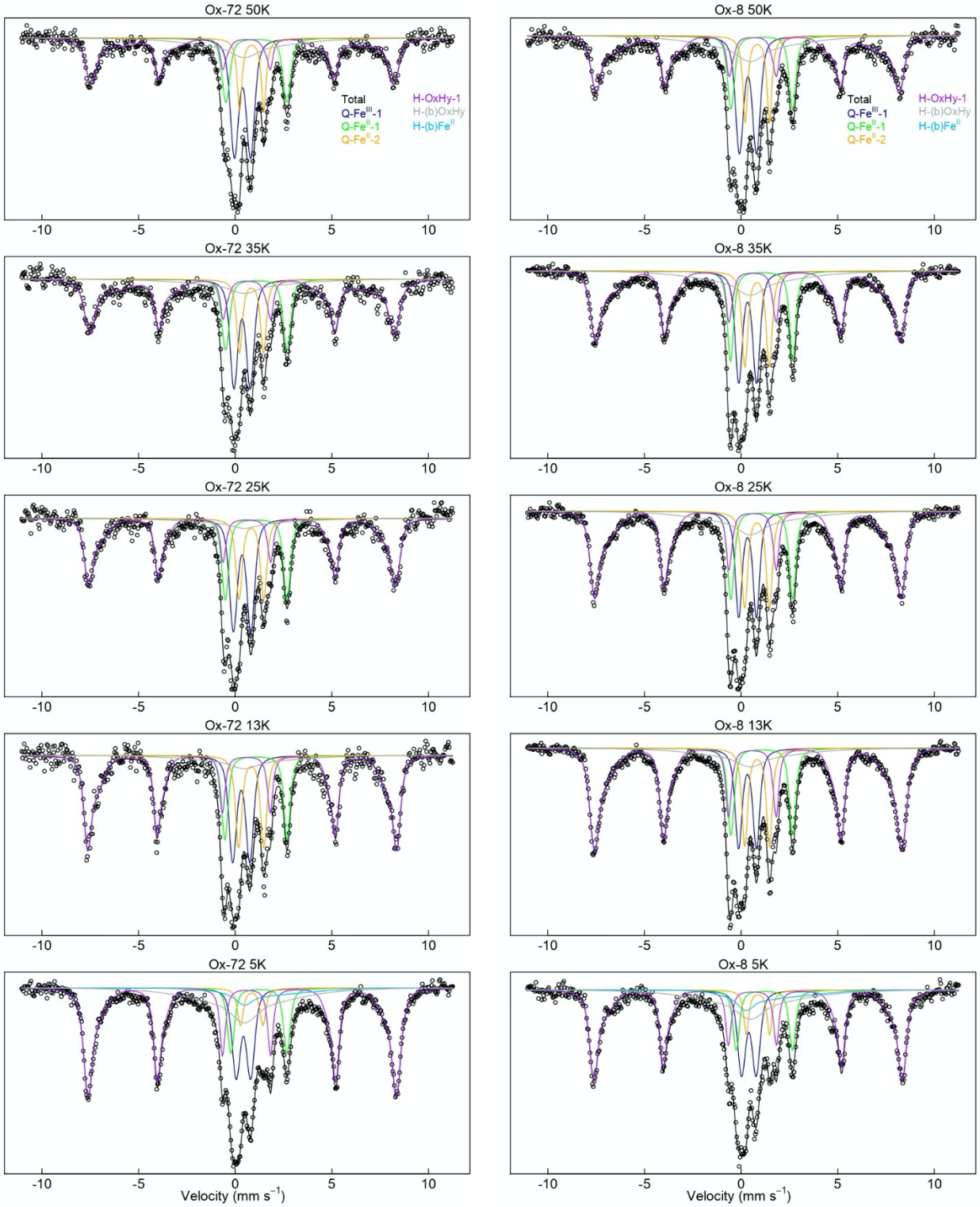

Figure 4. Mössbauer spectra (50 K, 35 K, 25 K, 13 K, 5 K) for soils collected at the end of the last (third) oxic interval, for the redox oscillation treatments Ox-72 and Ox-8. For each spectrum,

the black line corresponds to the total calculated fit, through the discrete data points. The resolved spectral components and assignments are: (1) **Q-Fe^{III}-1,** the deep central doublet (blue line) corresponding to Fe^{III} in aluminosilicates or organic matter; (2) **QFe^{II}-1**, the wider ferrous doublet corresponding to adsorbed Fe^{II} or Fe^{II} in clays or organic matter (green line); (3) **Q-Fe^{II}-2** the narrow ferrous doublet corresponding to ilmenite (brown line); (4) **HFD-OxHy-1**, the dominant sextet (purple line) corresponding to Fe^{III}-oxyhydroxides that are magnetically ordered; (5) **HFD-(b)OxHy** the collapsed 'sextet' corresponding to Fe^{III} oxyhyroxides near their blocking temperature; and (6) H-(b)Fe^{II} partially magnetically ordered Fe^{II} phase. Detailed fitting parameters are provided in the Supplementary Material (Table S3 and S6).

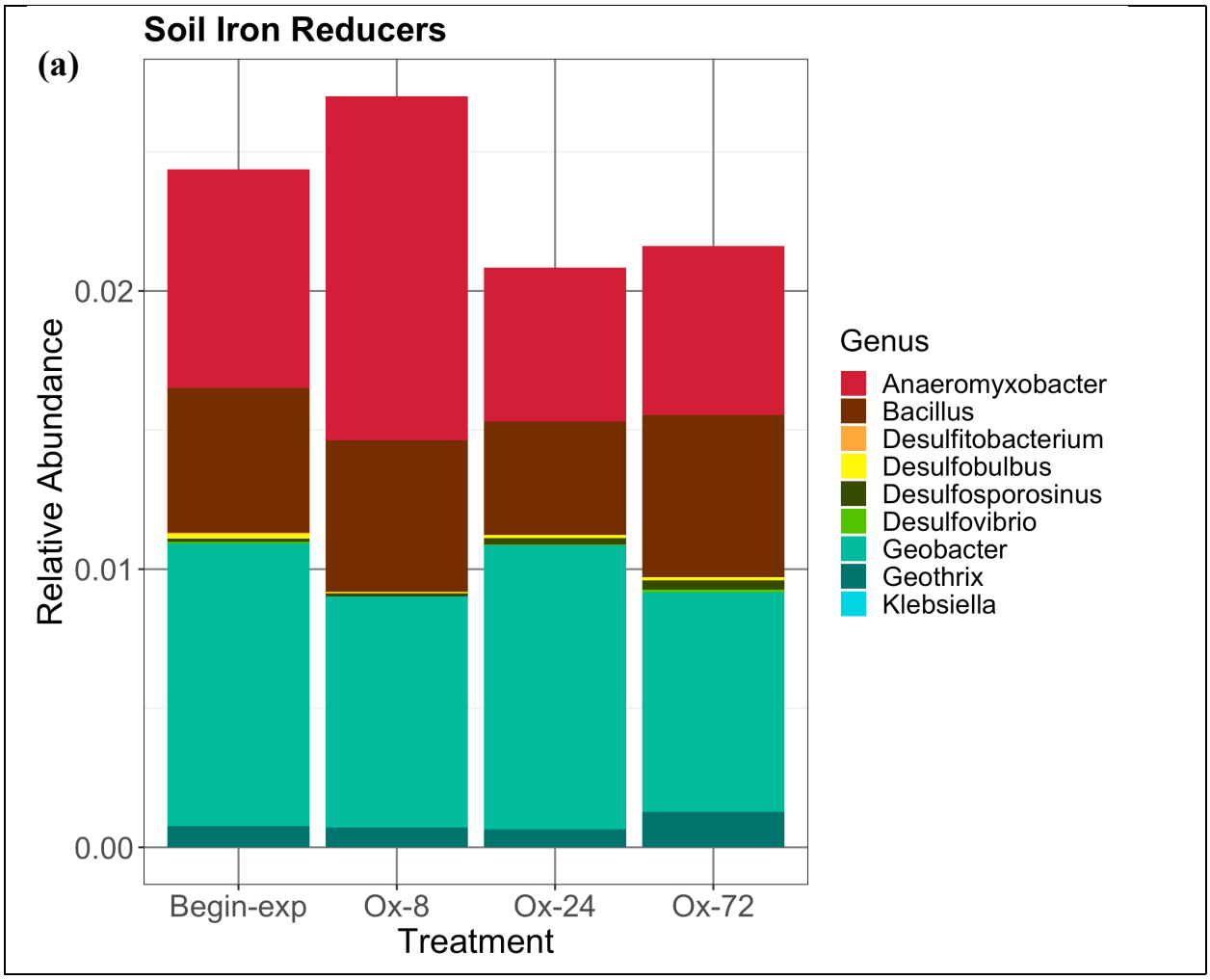
(a)
Soil Iron Reducers
Relative Abundance
0.02
0.01
0.00
Begin-exp
Ox-8
Ox-24
Ox-72
Treatment
Genus
Anaeromyxobacter
Bacillus
Desulfitobacterium
Desulfobulbus
Desulfosporosinus
Desulfovibrio
Geobacter
Geothrix
Klebsiella

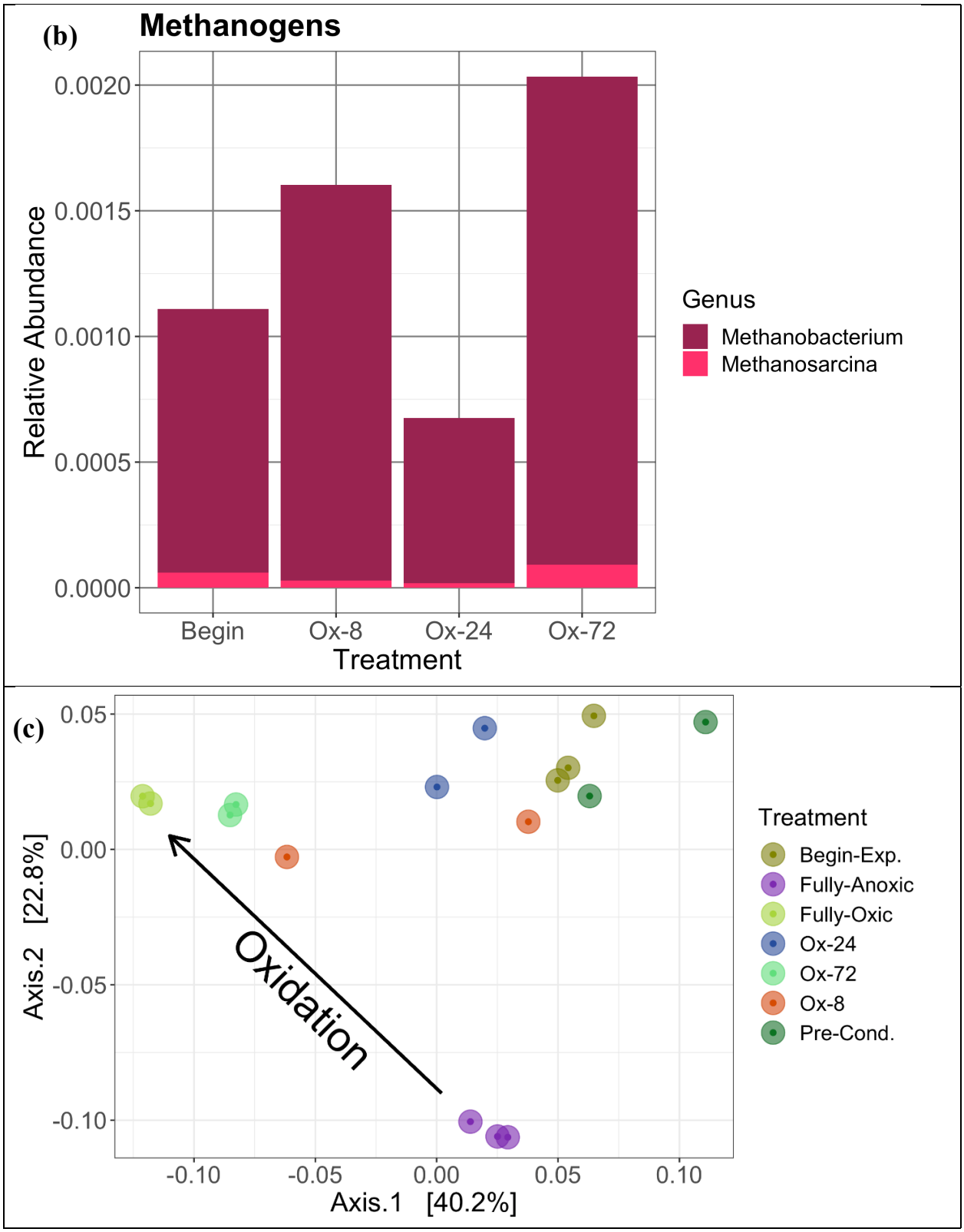

Figure 5. Soil microbial composition for iron-reducers (a) and methanogens (b) composition sampled in the last/third anoxic event for treatments Ox-72 and Ox-8 (with long and short

preceding oxidation exposure). (c) Principal coordinates analysis (PCoA) of microbial community 16S gene for all treatments evidencing a separation in microbial populations according to the preceding oxidation time (τ_{oxic}) for the redox oscillation treatments.

REFERENCES

494 1. Lin, Y.; Campbell, A. N.; Bhattacharyya, A.; DiDonato, N.; Thompson, A. M.; Tfaily, M. M.; Nico, P. S.; Silver, W. L.; Pett-Ridge, J., Differential effects of redox conditions on the
496 decomposition of litter and soil organic matter. *Biogeochemistry* **2021,** *154*, (1), 1-15.
2. Wood, T. E.; Detto, M.; Silver, W. L., Sensitivity of Soil Respiration to Variability in
498 Soil Moisture and Temperature in a Humid Tropical Forest. *PLOS ONE* **2013,** *8*, (12), e80965.
3. Zakem, E. J.; Polz, M. F.; Follows, M. J., Redox-informed models of global
500 biogeochemical cycles. *Nature Communications* **2020,** *11*, (1), 5680.
4. Peiffer, S.; Kappler, A.; Haderlein, S. B.; Schmidt, C.; Byrne, J. M.; Kleindienst, S.;
502 Vogt, C.; Richnow, H. H.; Obst, M.; Angenent, L. T.; Bryce, C.; McCammon, C.; Planer-Friedrich, B., A biogeochemical–hydrological framework for the role of redox-active compounds
504 in aquatic systems. *Nature Geoscience* **2021,** *14*, (5), 264-272.
5. Levar, C. E.; Hoffman, C. L.; Dunshee, A. J.; Toner, B. M.; Bond, D. R., Redox potential
506 as a master variable controlling pathways of metal reduction by geobacter sulfurreducens. *ISME J* **2017,** *11*.
508 6. Chen, C.; Hall, S. J.; Coward, E.; Thompson, A., Iron-mediated organic matter decomposition in humid soils can counteract protection. *Nature Communications* **2020,** *11*, (1),
510 2255.
7. Keiluweit, M.; Gee, K.; Denney, A.; Fendorf, S., Anoxic microsites in upland soils
512 dominantly controlled by clay content. *Soil Biol Biochem* **2018,** *118*.
8. Wanzek, T.; Keiluweit, M.; Baham, J.; Dragila, M. I.; Fendorf, S.; Fiedler, S.; Nico, P.
514 S.; Kleber, M., Quantifying biogeochemical heterogeneity in soil systems. *Geoderma* **2018,** *324*, 89-97.
516 9. Keiluweit, M.; Nico, P. S.; Kleber, M.; Fendorf, S., Are oxygen limitations under recognized regulators of organic carbon turnover in upland soils? *Biogeochemistry* **2016,** *127*, (2-
518 3), 157-171.
10. LaCroix, R. E.; Tfaily, M. M.; McCreight, M.; Jones, M. E.; Spokas, L.; Keiluweit, M.,
520 Shifting mineral and redox controls on carbon cycling in seasonally flooded mineral soils. *Biogeosciences* **2019,** *16*, (13), 2573-2589.
522 11. Chen, C.; Barcellos, D.; Richter, D. D.; Schroeder, P. A.; Thompson, A., Redoximorphic Bt horizons of the Calhoun CZO soils exhibit depth-dependent iron-oxide crystallinity. *Journal*
524 *of Soils and Sediments* **2019**.
12. Growle, A. J.; Lueker, D. C.; Gaskill, H. S., Periodic (Liesegang) Precipitation of
526 Chemicals. *Nature* **1963,** *199*, (4893), 623-624.
13. Gasparatos, D.; Tarenidis, D.; Haidouti, C.; Oikonomou, G., Microscopic structure of soil
528 Fe-Mn nodules: environmental implication. *Environmental Chemistry Letters* **2005,** *2*, (4), 175-178.
530 14. Barcellos, D.; Cyle, K. T.; Thompson, A., Faster redox fluctuations can lead to higher iron reduction rates in humid forest soils. *Biogeochemistry* **2018,** *137*, (3), 367-378.
532 15. Liptzin, D.; Silver, W. L.; Detto, M., Temporal Dynamics in Soil Oxygen and Greenhouse Gases in Two Humid Tropical Forests. *Ecosystems* **2011,** *14*, (2), 171-182.
534 16. Hall, S. J.; McDowell, W. H.; Silver, W. L., When wet gets wetter: decoupling of moisture, redox biogeochemistry, and greenhouse gas fluxes in a humid tropical forest soil.
536 *Ecosystems* **2013,** *16*, (4), 576-589.

17. Barcellos, D.; O'Connell, C.; Silver, W.; Meile, C.; Thompson, A., Hot Spots and Hot Moments of Soil Moisture Explain Fluctuations in Iron and Carbon Cycling in a Humid Tropical Forest Soil. *Soil Systems* **2018,** *2*, (4), 59.
18. DeAngelis, K. M.; Silver, W. L.; Thompson, A. W.; Firestone, M. K., Microbial communities acclimate to recurring changes in soil redox potential status. *Environmental Microbiology* **2010,** *12*, (12), 3137-3149.
19. Bhattacharyya, A.; Campbell, A. N.; Tfaily, M. M.; Lin, Y.; Kukkadapu, R. K.; Silver, W. L.; Nico, P. S.; Pett-Ridge, J., Redox Fluctuations Control the Coupled Cycling of Iron and Carbon in Tropical Forest Soils. *Environmental Science & Technology* **2018**.
20. Pett-Ridge, J.; Silver, W. L.; Firestone, M. K., Redox fluctuations frame microbial community impacts on N-cycling rates in a humid tropical forest soil. *Biogeochemistry* **2006,** *81*, (1), 95-110.
21. Pett-Ridge, J.; Petersen, D. G.; Nuccio, E.; Firestone, M. K., Influence of oxic/anoxic fluctuations on ammonia oxidizers and nitrification potential in a wet tropical soil. *FEMS Microbiology Ecology* **2013,** *85*, (1), 179-194.
22. Pett-Ridge, J. Rapidly fluctuating redox regimes frame the ecology of microbial communities and their biogeochemical function in a humid tropical soil. Doctoral Dissertation, University of California - Berkeley, Berkeley, CA, USA, 2005.
23. Calabrese, S.; Barcellos, D.; Thompson, A.; Porporato, A., Theoretical Constraints on Fe Reduction Rates in Upland Soils as a Function of Hydroclimatic Conditions. *Journal of Geophysical Research: Biogeosciences* **2020,** *125*, (12), e2020JG005894.
24. Zhang, Z.; Furman, A., Soil redox dynamics under dynamic hydrologic regimes - A review. *Science of The Total Environment* **2021,** *763*, 143026.
25. Bonaiuti, S.; Blodau, C.; Knorr, K.-H., Transport, anoxia and end-product accumulation control carbon dioxide and methane production and release in peat soils. *Biogeochemistry* **2017,** *133*, (2), 219-239.
26. Chen, C.; Meile, C.; Wilmoth, J. L.; Barcellos, D.; Thompson, A., Influence of pO2 on Iron Redox Cycling and Anaerobic Organic Carbon Mineralization in a Humid Tropical Forest Soil. *Environmental Science & Technology* **2018**.
27. Ginn, B.; Meile, C.; Wilmoth, J.; Tang, Y.; Thompson, A., Rapid Iron Reduction Rates Are Stimulated by High-Amplitude Redox Fluctuations in a Tropical Forest Soil. *Environmental Science & Technology* **2017,** *51*, (6), 3250-3259.
28. Wilmoth, J. L.; Moran, M. A.; Thompson, A., Transient O2 pulses direct Fe crystallinity and Fe(III)-reducer gene expression within a soil microbiome. *Microbiome* **2018,** *6*, (1), 189.
29. Gabriel, G. V. M.; Oliveira, L. C.; Barros, D. J.; Bento, M. S.; Neu, V.; Toppa, R. H.; Carmo, J. B.; Navarrete, A. A., Methane emission suppression in flooded soil from Amazonia. *Chemosphere* **2020,** *250*, 126263.
30. Angle, J. C.; Morin, T. H.; Solden, L. M.; Narrowe, A. B.; Smith, G. J.; Borton, M. A.; Rey-Sanchez, C.; Daly, R. A.; Mirfenderesgi, G.; Hoyt, D. W.; Riley, W. J.; Miller, C. S.; Bohrer, G.; Wrighton, K. C., Methanogenesis in oxygenated soils is a substantial fraction of wetland methane emissions. *Nature Communications* **2017,** *8*, (1), 1567.
31. Teh, Y. A.; Dubinsky, E. A.; Silver, W. L.; Carlson, C. M., Suppression of methanogenesis by dissimilatory Fe (III)-reducing bacteria in tropical rain forest soils: Implications for ecosystem methane flux. *Global Change Biology* **2008,** *14*, (2), 413-422.

32. Hu, J.; Wu, H.; Sun, Z.; Peng, Q.-a.; Zhao, J.; Hu, R., Ferrous iron (Fe2+) addition decreases methane emissions induced by rice straw in flooded paddy soils. *ACS Earth and Space Chemistry* **2020**.
33. Sivan, O.; Shusta, S.; Valentine, D., Methanogens rapidly transition from methane production to iron reduction. *Geobiology* **2016,** *14*, (2), 190-203.
34. Lovley, D. R.; Phillips, E. J., Novel mode of microbial energy metabolism: organic carbon oxidation coupled to dissimilatory reduction of iron or manganese. *Applied and environmental microbiology* **1988,** *54*, (6), 1472-1480.
35. LaRowe, D. E.; Van Cappellen, P., Degradation of natural organic matter: a thermodynamic analysis. *Geochim Cosmochim Acta* **2011,** *75*.
36. Roden, E. E., Microbial iron-redox cycling in subsurface environments. *Biochem Soc Trans* **2012,** *40*.
37. Boye, K.; Noël, V.; Tfaily, M. M.; Bone, S. E.; Williams, K. H.; Bargar, John R.; Fendorf, S., Thermodynamically controlled preservation of organic carbon in floodplains. *Nature Geoscience* **2017,** *10*, (6), 415-419.
38. Keiluweit, M.; Wanzek, T.; Kleber, M.; Nico, P.; Fendorf, S., Anaerobic microsites have an unaccounted role in soil carbon stabilization. *Nature Communications* **2017,** *8*, (1), 1771.
39. Laio, F.; Porporato, A.; Ridolfi, L.; Rodriguez-Iturbe, I., Plants in water-controlled ecosystems: active role in hydrologic processes and response to water stress: II. Probabilistic soil moisture dynamics. *Advances in Water Resources* **2001,** *24*, (7), 707-723.
40. Pett-Ridge, J.; Firestone, M., Redox fluctuation structures microbial communities in a wet tropical soil. *Applied and environmental microbiology* **2005,** *71*, (11), 6998-7007.
41. Mason-Jones, K.; Robinson, S. L.; Veen, G. F.; Manzoni, S.; van der Putten, W. H., Microbial storage and its implications for soil ecology. *The ISME Journal* **2021**.
42. Conrad, R., Soil microorganisms as controllers of atmospheric trace gases (H2, CO, CH4, OCS, N2O, and NO). *Microbiological Reviews* **1996,** *60*, (4), 609-640.
43. Roden, E. E., Diversion of Electron Flow from Methanogenesis to Crystalline Fe(III) Oxide Reduction in Carbon-Limited Cultures of Wetland Sediment Microorganisms. *Applied and Environmental Microbiology* **2003,** *69*, (9), 5702.
44. Bar-Or, I.; Elvert, M.; Eckert, W.; Kushmaro, A.; Vigderovich, H.; Zhu, Q.; Ben-Dov, E.; Sivan, O., Iron-Coupled Anaerobic Oxidation of Methane Performed by a Mixed Bacterial-Archaeal Community Based on Poorly Reactive Minerals. *Environmental science & technology* **2017,** *51*, (21), 12293-12301.
45. Ettwig, K. F.; Zhu, B.; Speth, D.; Keltjens, J. T.; Jetten, M. S.; Kartal, B., Archaea catalyze iron-dependent anaerobic oxidation of methane. *Proceedings of the National Academy of Sciences* **2016,** *113*, (45), 12792-12796.
46. Blazewicz, S. J.; Petersen, D. G.; Waldrop, M. P.; Firestone, M. K., Anaerobic oxidation of methane in tropical and boreal soils: Ecological significance in terrestrial methane cycling. *Journal of Geophysical Research: Biogeosciences* **2012,** *117*, (G2).
47. Ginn, B. R.; Habteselassie, M. Y.; Meile, C.; Thompson, A., Effects of sample storage on microbial Fe-reduction in tropical rainforest soils. *Soil Biology and Biochemistry* **2014,** *68*, 44-51.
48. Peretyazhko, T.; Sposito, G., Iron (III) reduction and phosphorous solubilization in humid tropical forest soils. *Geochimica et Cosmochimica Acta* **2005,** *69*, (14), 3643-3652.

49. Barcellos, D. Biogeochemical cycling of iron and carbon in humid (sub)tropical forest soils under fluctuating redox conditions. Doctoral Dissertation, University of Georgia, Athens, GA, USA, 2018.
50. Thompson, A.; Chadwick, O. A.; Rancourt, D. G.; Chorover, J., Iron-oxide crystallinity increases during soil redox oscillations. *Geochimica et Cosmochimica Acta* **2006,** *70*, (7), 1710-1727.
51. Caporaso, J. G.; Lauber, C. L.; Walters, W. A.; Berg-Lyons, D.; Huntley, J.; Fierer, N.; Owens, S. M.; Betley, J.; Fraser, L.; Bauer, M.; Gormley, N.; Gilbert, J. A.; Smith, G.; Knight, R., Ultra-high-throughput microbial community analysis on the Illumina HiSeq and MiSeq platforms. *The ISME Journal* **2012,** *6*, (8), 1621-1624.
52. Caporaso, J. G.; Kuczynski, J.; Stombaugh, J.; Bittinger, K.; Bushman, F. D.; Costello, E. K.; Fierer, N.; Peña, A. G.; Goodrich, J. K.; Gordon, J. I.; Huttley, G. A.; Kelley, S. T.; Knights, D.; Koenig, J. E.; Ley, R. E.; Lozupone, C. A.; McDonald, D.; Muegge, B. D.; Pirrung, M.; Reeder, J.; Sevinsky, J. R.; Turnbaugh, P. J.; Walters, W. A.; Widmann, J.; Yatsunenko, T.; Zaneveld, J.; Knight, R., QIIME allows analysis of high-throughput community sequencing data. *Nature Methods* **2010,** *7*, (5), 335-336.
53. Callahan, B. J.; McMurdie, P. J.; Rosen, M. J.; Han, A. W.; Johnson, A. J. A.; Holmes, S. P., DADA2: High-resolution sample inference from Illumina amplicon data. *Nature Methods* **2016,** *13*, (7), 581-583.
54. Halekoh, U.; Højsgaard, S., A kenward-roger approximation and parametric bootstrap methods for tests in linear mixed models–the R package pbkrtest. *Journal of Statistical Software* **2014,** *59*, (9), 1-30.
55. Bates, D.; Mächler, M.; Bolker, B.; Walker, S., Fitting Linear Mixed-Effects Models Using lme4. *Journal of Statistical Software* **2015,** *67*, (1), 48.
56. Hall, S. J.; Silver, W. L., Reducing conditions, reactive metals, and their interactions can explain spatial patterns of surface soil carbon in a humid tropical forest. *Biogeochemistry* **2015,** *125*, (2), 149-165.
57. Kappler, A.; Bryce, C.; Mansor, M.; Lueder, U.; Byrne, J. M.; Swanner, E. D., An evolving view on biogeochemical cycling of iron. *Nature Reviews Microbiology* **2021,** *19*, (6), 360-374.
58. Chen, C.; Thompson, A., Ferrous Iron Oxidation under Varying pO2 Levels: The Effect of Fe (III)/Al (III) Oxide Minerals and Organic Matter. *Environmental Science & Technology* **2018,** *52*, (2), 597-606.
59. Schwaminger, S. P.; Surya, R.; Filser, S.; Wimmer, A.; Weigl, F.; Fraga-García, P.; Berensmeier, S., Formation of iron oxide nanoparticles for the photooxidation of water: Alteration of finite size effects from ferrihydrite to hematite. *Scientific Reports* **2017,** *7*, (1), 12609.
60. Hu, Y.; Li, Q.; Lee, B.; Jun, Y.-S., Aluminum affects heterogeneous Fe (III)(Hydr) oxide nucleation, growth, and ostwald ripening. *Environmental science & technology* **2013,** *48*, (1), 299-306.
61. Becking, L. G. M. B.; Kaplan, I. R.; Moore, D., Limits of the Natural Environment in Terms of pH and Oxidation-Reduction Potentials. *The Journal of Geology* **1960,** *68*, (3), 243-284.
62. Gambrell, R. P.; DeLaune, R. D.; Patrick Jr, W. H., Redox processes in soils following oxygen depletion. *Plant Life Under Oxygen Deprivation. SPB Academic Publishing BV, The Hague, The Netherlands* **1991**, 101-117.

63. Suriyavirun, N.; Krichels, A. H.; Kent, A. D.; Yang, W. H., Microtopographic differences in soil properties and microbial community composition at the field scale. *Soil Biology and Biochemistry* **2019,** *131*, 71-80.
64. Lin, W. C.; Coppi, M. V.; Lovley, D. R., Geobacter sulfurreducens Can Grow with Oxygen as a Terminal Electron Acceptor. *Applied and Environmental Microbiology* **2004,** *70*, (4), 2525-2528.
65. Hall, S. J.; Liptzin, D.; Buss, H. L.; DeAngelis, K.; Silver, W. L., Drivers and patterns of iron redox cycling from surface to bedrock in a deep tropical forest soil: a new conceptual model. *Biogeochemistry* **2016,** *130*, (1-2), 177-190.
66. Hall, S. J.; Silver, W. L., Iron oxidation stimulates organic matter decomposition in humid tropical forest soils. *Global change biology* **2013,** *19*, (9), 2804-2813.
67. Lin, Y.; Bhattacharyya, A.; Campbell, A. N.; Nico, P. S.; Pett-Ridge, J.; Silver, W. L., Phosphorus Fractionation Responds to Dynamic Redox Conditions in a Humid Tropical Forest Soil. *Journal of Geophysical Research: Biogeosciences* **2018,** *123*, (9), 3016-3027.
68. Queiroz, H. M.; Ferreira, T. O.; Barcellos, D.; Nóbrega, G. N.; Antelo, J.; Otero, X. L.; Bernardino, A. F., From sinks to sources: The role of Fe oxyhydroxide transformations on phosphorus dynamics in estuarine soils. *Journal of Environmental Management* **2021,** *278*, 111575.
69. Silver, W. L.; Lugo, A.; Keller, M., Soil oxygen availability and biogeochemistry along rainfall and topographic gradients in upland wet tropical forest soils. *Biogeochemistry* **1999,** *44*, (3), 301-328.
70. O'Connell, C. S.; Ruan, L.; Silver, W. L., Drought drives rapid shifts in tropical rainforest soil biogeochemistry and greenhouse gas emissions. *Nature communications* **2018,** *9*, (1), 1348.
71. Dubinsky, E. A.; Silver, W. L.; Firestone, M. K., Tropical forest soil microbial communities couple iron and carbon biogeochemistry. *Ecology* **2010,** *91*, (9), 2604-2612.
72. Hall, S. J.; Berhe, A. A.; Thompson, A., Order from disorder: do soil organic matter composition and turnover co-vary with iron phase crystallinity? *Biogeochemistry* **2018,** *140*, (1), 93-110.
73. Lin, Y.; Gross, A.; O'Connell, C. S.; Silver, W. L., Anoxic conditions maintained high phosphorus sorption in humid tropical forest soils. *Biogeosciences* **2020,** *17*, (1), 89-101.
74. Roden, E. E.; Wetzel, R. G., Organic carbon oxidation and suppression of methane production by microbial Fe (III) oxide reduction in vegetated and unvegetated freshwater wetland sediments. *Limnology and Oceanography* **1996,** *41*, (8), 1733-1748.
75. Blazewicz, S. J.; Barnard, R. L.; Daly, R. A.; Firestone, M. K., Evaluating rRNA as an indicator of microbial activity in environmental communities: limitations and uses. *The ISME Journal* **2013,** *7*, (11), 2061-2068.
76. Liu, C.-T.; Miyaki, T.; Aono, T.; Oyaizu, H., Evaluation of Methanogenic Strains and Their Ability to Endure Aeration and Water Stress. *Current Microbiology* **2008,** *56*, (3), 214-218.
77. Horne, A. J.; Lessner, D. J., Assessment of the oxidant tolerance of Methanosarcina acetivorans. *FEMS Microbiology Letters* **2013,** *343*, (1), 13-19.
78. Watanabe, T.; Asakawa, S.; Hayano, K., Long-term submergence of non-methanogenic oxic upland field soils helps to develop the methanogenic archaeal community as revealed by pot and field experiments. *Pedosphere* **2020,** *30*, (1), 62-72.

79. Jasso-Chávez, R.; Santiago-Martínez, M. G.; Lira-Silva, E.; Pineda, E.; Zepeda-Rodríguez, A.; Belmont-Díaz, J.; Encalada, R.; Saavedra, E.; Moreno-Sánchez, R., Air-Adapted Methanosarcina acetivorans Shows High Methane Production and Develops Resistance against Oxygen Stress. *PLOS ONE* **2015,** *10*, (2), e0117331.
80. Wu, X. L.; Conrad, R., Functional and structural response of a cellulose-degrading methanogenic microbial community to multiple aeration stress at two different temperatures. *Environmental Microbiology* **2001,** *3*, (6), 355-362.
81. Fetzer, S.; Bak, F.; Conrad, R., Sensitivity of methanogenic bacteria from paddy soil to oxygen and desiccation. *FEMS Microbiology Ecology* **2006,** *12*, (2), 107-115.
82. Wagner, D.; Pfeiffer, E. M.; Bock, E., Methane production in aerated marshland and model soils: effects of microflora and soil texture. *Soil Biology and Biochemistry* **1999,** *31*, (7), 999-1006.
83. Valenzuela, E. I.; Prieto-Davó, A.; López-Lozano, N. E.; Hernández-Eligio, A.; Vega-Alvarado, L.; Juárez, K.; García-González, A. S.; López, M. G.; Cervantes, F. J., Anaerobic methane oxidation driven by microbial reduction of natural organic matter in a tropical wetland. *Applied and Environmental Microbiology* **2017,** *83*, (11), e00645-17.
84. Aromokeye, D. A.; Kulkarni, A. C.; Elvert, M.; Wegener, G.; Henkel, S.; Coffinet, S.; Eickhorst, T.; Oni, O. E.; Richter-Heitmann, T.; Schnakenberg, A.; Taubner, H.; Wunder, L.; Yin, X.; Zhu, Q.; Hinrichs, K.-U.; Kasten, S.; Friedrich, M. W., Rates and Microbial Players of Iron-Driven Anaerobic Oxidation of Methane in Methanic Marine Sediments. *Frontiers in Microbiology* **2020,** *10*, (3041).
85. Lovley, D. R., Happy together: microbial communities that hook up to swap electrons. *The ISME journal* **2017,** *11*, (2), 327.
86. Wegener, G.; Krukenberg, V.; Riedel, D.; Tegetmeyer, H. E.; Boetius, A., Intercellular wiring enables electron transfer between methanotrophic archaea and bacteria. *Nature* **2015,** *526*, (7574), 587.
87. He, Q.; Yu, L.; Li, J.; He, D.; Cai, X.; Zhou, S., Electron shuttles enhance anaerobic oxidation of methane coupled to iron(III) reduction. *Science of The Total Environment* **2019,** *688*, 664-672.
88. Rose, A. L.; Waite, T. D., Predicting iron speciation in coastal waters from the kinetics of sunlight-mediated iron redox cycling. *Aquatic Sciences* **2003,** *65*, (4), 375-383.
89. Lin, Y.; Gross, A.; Silver, W. L., Low Redox Decreases Potential Phosphorus Limitation on Soil Biogeochemical Cycling Along a Tropical Rainfall Gradient. *Ecosystems* **2021**.
90. Nóbrega, G. N.; Otero, X. L.; Macías, F.; Ferreira, T. O., Phosphorus geochemistry in a Brazilian semiarid mangrove soil affected by shrimp farm effluents. *Environmental Monitoring and Assessment* **2014,** *186*, (9), 5749-5762.
91. Huang, W.; Hall, S. J., Elevated moisture stimulates carbon loss from mineral soils by releasing protected organic matter. *Nature communications* **2017,** *8*, (1), 1774.
92. Couture, R.-M.; Charlet, L.; Markelova, E.; Madé, B. t.; Parsons, C. T., On–off mobilization of contaminants in soils during redox oscillations. *Environmental science & technology* **2015,** *49*, (5), 3015-3023.
93. Barcellos, D.; Queiroz, H. M.; Ferreira, A. D.; Bernardino, A. F.; Nóbrega, G. N.; Otero, X. L.; Ferreira, T. O., Short-term Fe reduction and metal dynamics in estuarine soils impacted by Fe-rich mine tailings. *Applied Geochemistry* **2021**, 105134.

760 94. Barcellos, D.; Jensen, S. S. K.; Bernardino, A. F.; Gabriel, F. A.; Ferreira, T. O.; Quintana, C. O., Benthic bioturbation: A canary in the mine for the retention and release of
762 metals from estuarine sediments. *Marine Pollution Bulletin* **2021,** *172*, 112912.
95. Borch, T.; Kretzschmar, R.; Kappler, A.; Cappellen, P. V.; Ginder-Vogel, M.; Voegelin,
764 A.; Campbell, K., Biogeochemical redox processes and their impact on contaminant dynamics. *Environmental Science & Technology* **2009,** *44*, (1), 15-23.

766

Supplementary material

The Pattern of Temporal Redox Shifts Can Determine If Anaerobic Fe^{II} or CH_4 Production Dominates

Diego Barcellos[1,2], Ashley Campbell[3,4], Jennifer Pett-Ridge[3], and Aaron Thompson[1*]

[1]*Department of Crop and Soil Sciences, University of Georgia. Athens, GA 30605, USA*
[2]*Department of Environmental Sciences. Federal University of São Paulo (UNIFESP). Diadema, SP 09972, Brazil*
[3]*Lawrence Livermore National Laboratory. Livermore, CA 94550, USA*
[4] *Life & Environmental Sciences Department, University of California Merced, Merced, CA 95343, USA*

*Corresponding author: Aaron Thompson, University of Georgia, Department of Crop and Soil Sciences, Athens, GA 30602, AaronT@uga.edu

SECTION 1

MÖSSBAUER SPECTROSCOPY FOR THE SOILS UNDER REDOX OSCILLATIONS

The details regarding the analysis for Mössbauer Spectroscopy was adapted from Chen, et al. [1], at the temperatures 50 K, 35 K, 25 K, 13 K, and 5 K. For the soil samples collected at the end of the last (third) oxic interval of the treatments Ox-72, Ox-24, Ox-8, and for the soil at the beginning of the experiment (initial soil), we performed Mössbauer spectral fitting by using the Voigt-based fitting method of Rancourt and Ping [2] as implemented in the Recoil^{TM} software. For each Fe mineral phase, the relative abundance was obtained from the spectral fitting as a fraction of the total Fe spectral area. All errors for Mossbauer fitting parameters were acquired as two-standard deviation (2σ) errors, computed by Recoil^{TM}. This presumes equal Mossbauer recoilless fractions to compute the abundance of all Fe phases detected.

The Mössbauer spectra represents a Fe-bearing solid phase or correlates to a cluster of unresolved solid phase-Fe. The spectral components may form a doublet, sextet, octet, or a collapsed sextet, which indicates a solid phase near the temperature for magnetic ordering temperature (T_N). Solid phase-Fe display an intermediate shape between a doublet and full sextet at the temperature near T_N, filling the area between the superior baseline and the inverse depressions of the peaks. Our approach was to use a separate collapsed sextet component (containing exceedingly large line widths and Bhf = 0 T).

Across the five collected temperatures (50 K, 35 K, 25 K, 13 K, and 5 K), we determined six distinct spectral components. The resolved spectral components and assignments are the following: (1) **Q-Fe^{III}-1,** the deep central doublet, corresponding to Fe^{III} in aluminosilicates or organic matter; (2) **QFe^{II}-1**, the wide ferrous doublet corresponding to adsorbed Fe^{II} or Fe^{II} in clays/organic matter (green line); (3) **Q-Fe^{II}-2** the narrow ferrous doublet corresponding to Fe^{II} in ilmenite (brown line); (4) **HFD-OxHy-1**, the dominant sextet, corresponding to Fe^{III}-oxyhydroxides that are magnetically ordered; (5) **HFD-(b)OxHy** the collapsed 'sextet', corresponding to Fe^{III} oxyhyroxides near their blocking temperature; and (6) H-(b)Fe^{II} partially magnetically ordered Fe^{II} phase. Mössbauer spectra for each sample are presented in Figures S3 to S6, and detailed fitting parameters are provided in Tables S2 to S5.

SECTION 2

METHODS FOR MICROBIAL ANALYSIS

DNA extraction

DNA was extracted from soil slurry in duplicates following a modified phenol chloroform nucleic acid extraction method as follows. In lysing matrix E tubes, 0.25g of soil slurry was combined with 0.5 mL Extraction buffer (350mM K-PO_4, 0.7M NaCl, 50mM EDTA), 0.5 mL equilibrated phenol:chloroform:isoamyl alcohol (25:24:1, pH8), 30uL β-Me, and 20uL BSA (400mg/mL). Cells were lysed via bead beating on Fast-prep for 45 sec at 6.5 m s^{-1}. NaCl (0.7M final) and CTAB/NaCl (added at 1:10 volume) were added and vortexed. Tubes were cooled tubes on ice for 1 min and centrifuged for 5 min at 16,000 x *g* at 4°C. Aqueous layer was transferred to new 2mL microfuge tube and reserved on ice. Soils were then back extracted by adding 85 uL 5M NaCl and 0.5 mL Extraction Buffer to soil pellet. Samples were vortexed to mix well and centrifuged for 5 min at 16,000 x *g* at 4°C. Aqueous layer was removed and pooled with first aqueous layer collected. Aqueous layer was washed 1:1 with chloroform:isoamyl alcohol (24:1) and emulsified via vortexing for 15s followed by centrifugation for 5 min at 16,000 x *g* at 4°C. The new aqueous layer was transferred to a new 2 mL tube. Nucleic acids were recovered by adding 40% PEG/1.6M NaCl to the 2ml tube, mixed by inversion (~10 times) and incubated at 4°C (on ice) for 2 hours. After cold incubation, samples were centrifuged 30 min at 16,000 x *g* at 4°C. Nucleic acid pellet was washed twice with by vortexing with 1 mL 70% ice cold ethanol followed by centrifugation for 10 min at 16,000 x *g* at 4°C and decanting. Nucleic acid pellets were air dried and resuspended in 50 µL TE.

Sequencing

Extracted DNA from the samples were submitted for 16S gene sequencing at Argonne National Laboratory Next Generation Sequencing Core Facility. ANL Core Facility generated 16S amplicons using custom barcoded 515f-806r primers designed by Caporaso, et al. [3]. All samples were multiplexed and paired end sequencing (2x250) was performed on the MiSeq (Illumina).

Analysis

Sequence reads were demultiplexed (split_libraries_fastq.py) using Qiime (v1.9.1)[4] via MacQiime v1.9.1. Sequences were then quality controlled using the dada2 framework[5]. Briefly, sequences were length trimmed based on quality profiles, then sequences with max number of 'N' > 0 and/or maxed expected error > 2 were removed. Then paired reads were merged and collated into an OTU table. Finally, chimeras were removed and taxonomy was assigned using Silva v132 (nr) taxonomy reference database[6]. Quality controlled sequences were aligned using Muscle (v3.8.31)[7], then used to build a phylogenetic tree using FastTree (v2.1.10)[8].

The OTU table and taxonomy table generated in dada2, the phylogenetic tree and associated metadata were used to create a Phyloseq (v3.7)[9] object in R (v3.4.1)[10] (http://www.R-project.org/). Sample libraries with less than 8,000 reads were removed from the dataset and reads in remaining libraries were normalized using DeSeq2 v1.18.1 variance stabilization[11] R packages dplyr (v0.7.3)[12], vegan (v2.5-1)[13], and ggplot2 (v2.2.1)[14] were used for alpha and beta diversity analyses and statistical analyses.

SECTION 3

ACETATE ANALYSES BY NMR

For the collected aqueous phase samples at the end of the last (third) oxic interval for the treatments Ox-72, Ox-24, Ox-8, and Pre-Conditioning, metabolite analyses (acetate) were performed by Nuclear magnetic resonance spectroscopy (NMR). The aqueous extracts (180 uL) were diluted with perdeuterated sodium 4,4-dimethyl-4-silapentane-1-sulfonate (DSS-d6) in D_2O (5 mM, 20 uL). The resulting 0.5 mM dDSS (4,4-dimethyl-4-silapentane-1-sulfonic acid) in 10% D_2O/ 90% H_2O were used as an internal calibrant. The Varian Direct Drive 600-MHz NMR spectrometer (with a 5-mm triple resonance cold probe) was used to collect the NMR spectra for all samples. The samples were analyzed in 3 mm NMR tubes, with the temperature regulated at 298 K. Chemical shifts were due to the ^{1}H or ^{13}C methyl signals, in DSS-d6 at 0 ppm. The 90° ^{1}H pulse was calibrated before the measurement of each sample. The spectra for the one-dimensional ^{1}H were obtained with the Varian pulse sequence, containing a spectral width of 12 ppm and 512 transients. The acquisition time was 4 s, followed by a relaxation delay of 1.5 s during which pre-saturation of the water signal was applied, and the NOESY mixing time was 100 ms. Time domain free induction decays (57472 total points) were zero filled to 131072 total points prior to Fourier transform.

The 1D ^{1}H spectra were manually phased, baseline corrected, assigned metabolite identifications, and computed using Chenomx NMR Suite 8.3. The identification for each metabolite was performed by matching the chemical shift, J-coupling and intensity of experimental signals against compound signals in the Chenomx, Human Metabolome Database (HMDB) and custom in-house databases. Spectra were quantified based on intensity relative to the 0.5mM DSS-d6 (CAS-no 284664-85-3) internal standard. Spike-in amendments of acetate (ca. ~20 uM) were made into 4 representative samples to further confirm this metabolite identification.

SECTION 4

FIGURES AND TABLES

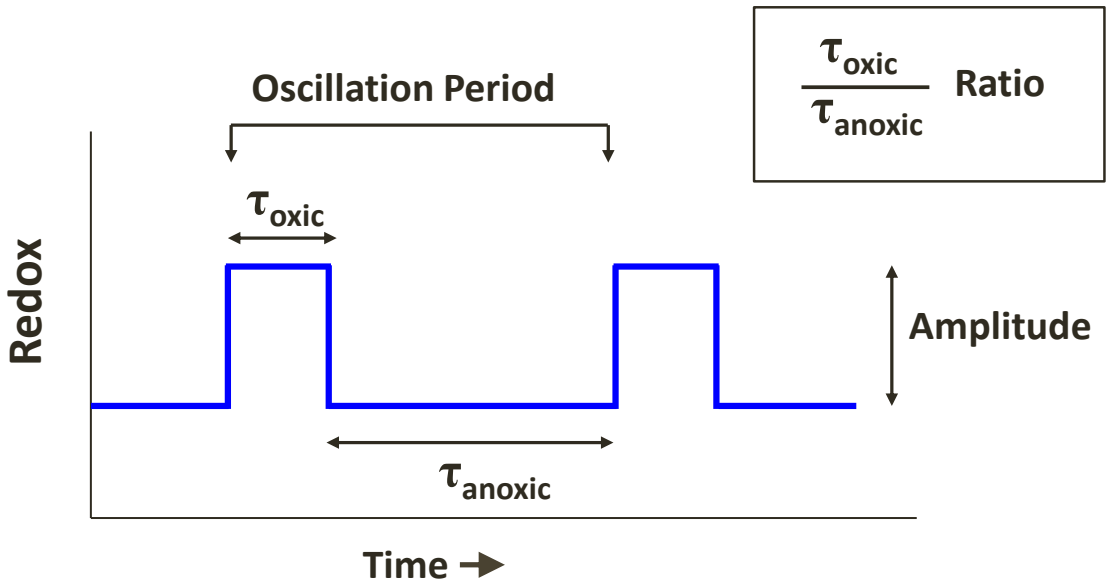

Figure S1 Components of a hypothetical redox oscillation cycle, proposed in Barcellos, et al. [15].

Figure S2. Soil sample sieved at 2 mm inside the 95%:5%:0% (N_2:H_2:O_2) glovebox Coy chamber. Soils from Bisley watershed (valley topographic position), Puerto Rico.

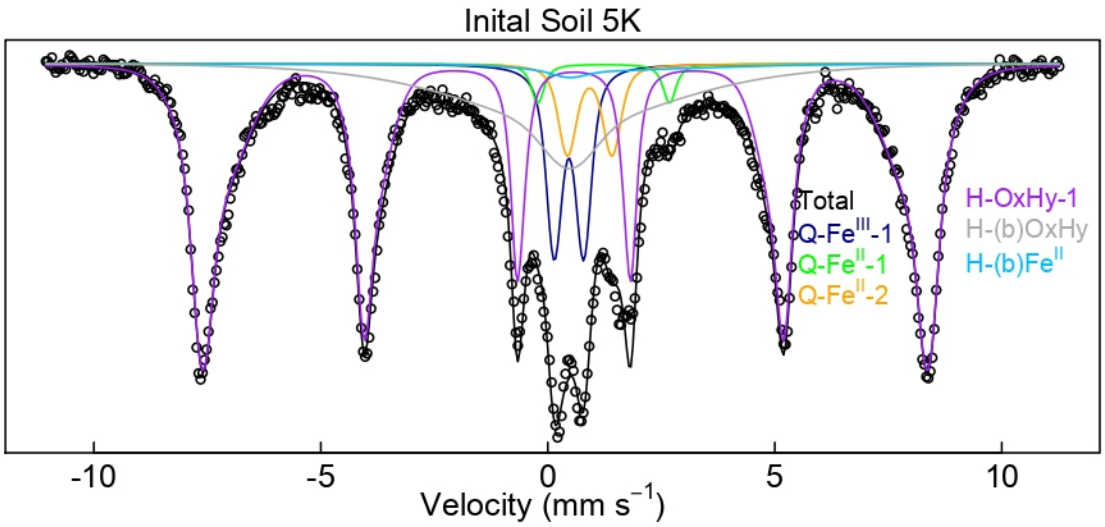

Figure S3. Mössbauer spectra (5 K) for the soil at the beginning of the redox oscillation experiment (initial soil). For each spectrum, the black line corresponds to the total calculated fit, through the discrete data points. Detailed fitting parameters are provided in the Table S3. The resolved spectral components and assignments are: (1) **Q-Fe^{III}-1,** the deep central doublet (blue line) corresponding to Fe^{III} in aluminosilicates or organic matter; (2) **QFe^{II}-1**, the wide ferrous doublet corresponding to adsorbed Fe^{II} or Fe^{II} in clays/organic matter (green line); (3) **Q-Fe^{II}-2** the narrow ferrous doublet corresponding to Fe^{II} in ilmenite (brown line); (4) **HFD-OxHy-1**, the dominant sextet (purple line) corresponding to Fe^{III}-oxyhydroxides that are magnetically ordered; (5) **HFD-(b)OxHy** the collapsed 'sextet' corresponding to Fe^{III} oxyhydroxides near their blocking temperature; and (6) H-(b)Fe^{II} partially magnetically ordered Fe^{II} phase.

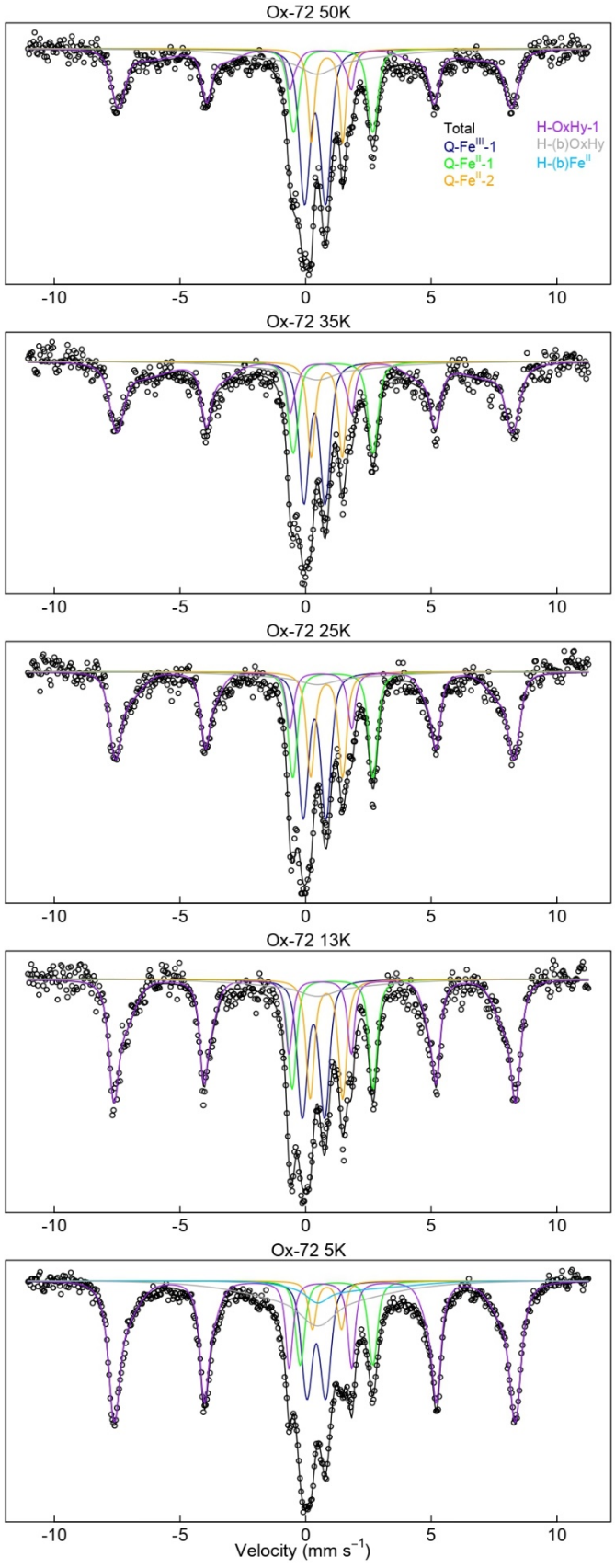

Figure S4. Mössbauer spectra (50 K, 35 K, 25 K, 13 K, 5 K) for soils collected at the end of the last (third) oxic interval, for the redox oscillation treatment **Ox-72** (oxygenation for 72 h). For each spectrum, the black line corresponds to the total calculated fit, through the discrete data points. Detailed fitting parameters are provided in the Supplementary Material (Table S4). The resolved spectral components and assignments are: (1) **Q-Fe^{III}-1,** the deep central doublet (blue line) corresponding to Fe^{III} in aluminosilicates or organic matter; (2) **QFe^{II}-1**, the wide ferrous doublet corresponding to adsorbed Fe^{II} or Fe^{II} in clays/organic matter (green line); (3) **Q-Fe^{II}-2** the narrow ferrous doublet corresponding to Fe^{II} in ilmenite (brown line); (4) **HFD-OxHy-1**, the dominant sextet (purple line) corresponding to Fe^{III}-oxyhydroxides that are magnetically ordered; (5) **HFD-(b)OxHy** the collapsed 'sextet' corresponding to Fe^{III} oxyhyroxides near their blocking temperature; and (6) H-(b)Fe^{II} partially magnetically ordered Fe^{II} phase.

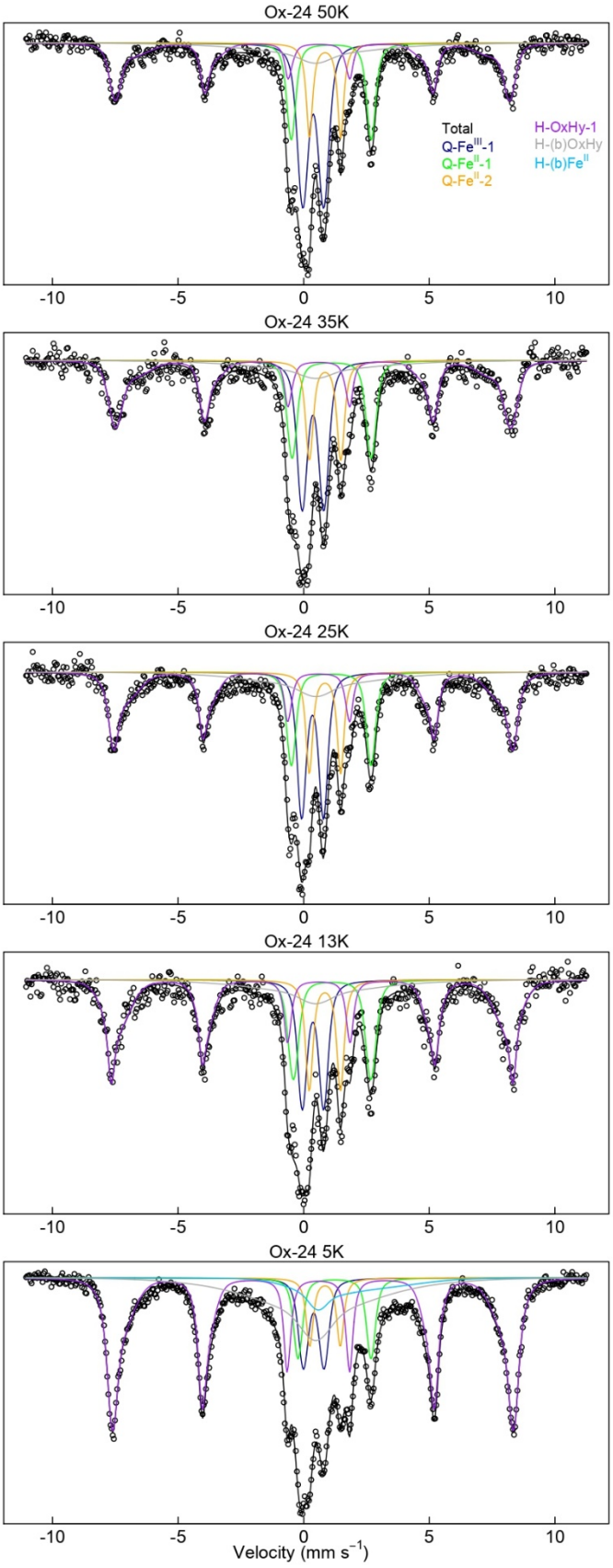

Figure S5. Mössbauer spectra (50 K, 35 K, 25 K, 13 K, 5 K) for soils collected at the end of the last (third) oxic interval, for the redox oscillation treatment **Ox-24** (oxygenation for 24 h). For each spectrum, the black line corresponds to the total calculated fit, through the discrete data points. Detailed fitting parameters are provided in the Supplementary Material (Table S5). The resolved spectral components and assignments are: (1) **Q-Fe^{III}-1,** the deep central doublet (blue line) corresponding to Fe^{III} in aluminosilicates or organic matter; (2) **QFe^{II}-1**, the wide ferrous doublet corresponding to adsorbed Fe^{II} or Fe^{II} in clays/organic matter (green line); (3) **Q-Fe^{II}-2** the narrow ferrous doublet corresponding to Fe^{II} in ilmenite (brown line); (4) **HFD-OxHy-1**, the dominant sextet (purple line) corresponding to Fe^{III}-oxyhydroxides that are magnetically ordered; (5) **HFD-(b)OxHy** the collapsed 'sextet' corresponding to Fe^{III} oxyhyroxides near their blocking temperature; and (6) H-(b)Fe^{II} partially magnetically ordered Fe^{II} phase.

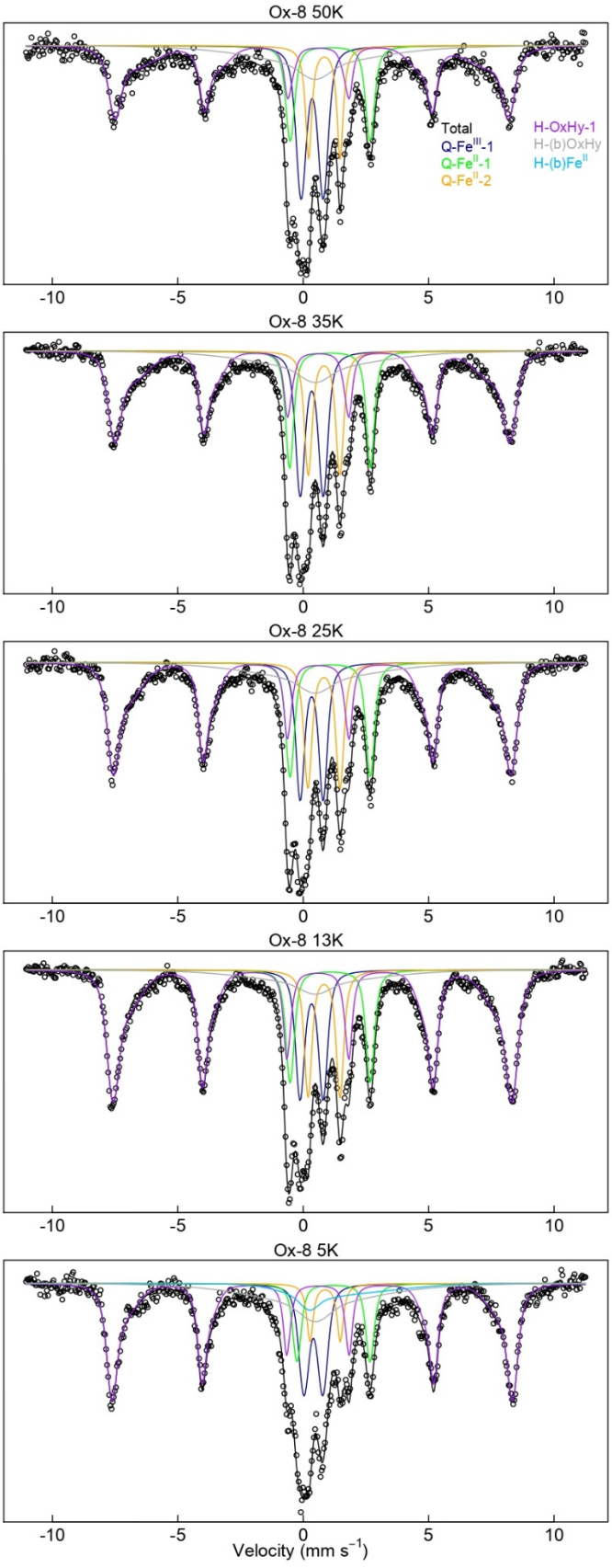

Figure S6. Mössbauer spectra (50 K, 35 K, 25 K, 13 K, 5 K) for soils collected at the end of the last (third) oxic interval, for the redox oscillation treatment **Ox-8** (oxygenation for 8 h). For each spectrum, the black line corresponds to the total calculated fit, through the discrete data points. Detailed fitting parameters are provided in the Supplementary Material (Table S6). The resolved spectral components and assignments are: (1) **Q-Fe^{III}-1,** the deep central doublet (blue line) corresponding to Fe^{III} in aluminosilicates or organic matter; (2) **QFe^{II}-1**, the wide ferrous doublet corresponding to adsorbed Fe^{II} or Fe^{II} in clays/organic matter (green line); (3) **Q-Fe^{II}-2** the narrow ferrous doublet corresponding to Fe^{II} in ilmenite (brown line); (4) **HFD-OxHy-1**, the dominant sextet (purple line) corresponding to Fe^{III}-oxyhydroxides that are magnetically ordered; (5) **HFD-(b)OxHy** the collapsed 'sextet' corresponding to Fe^{III} oxyhyroxides near their blocking temperature; and (6) H-(b)Fe^{II} partially magnetically ordered Fe^{II} phase.

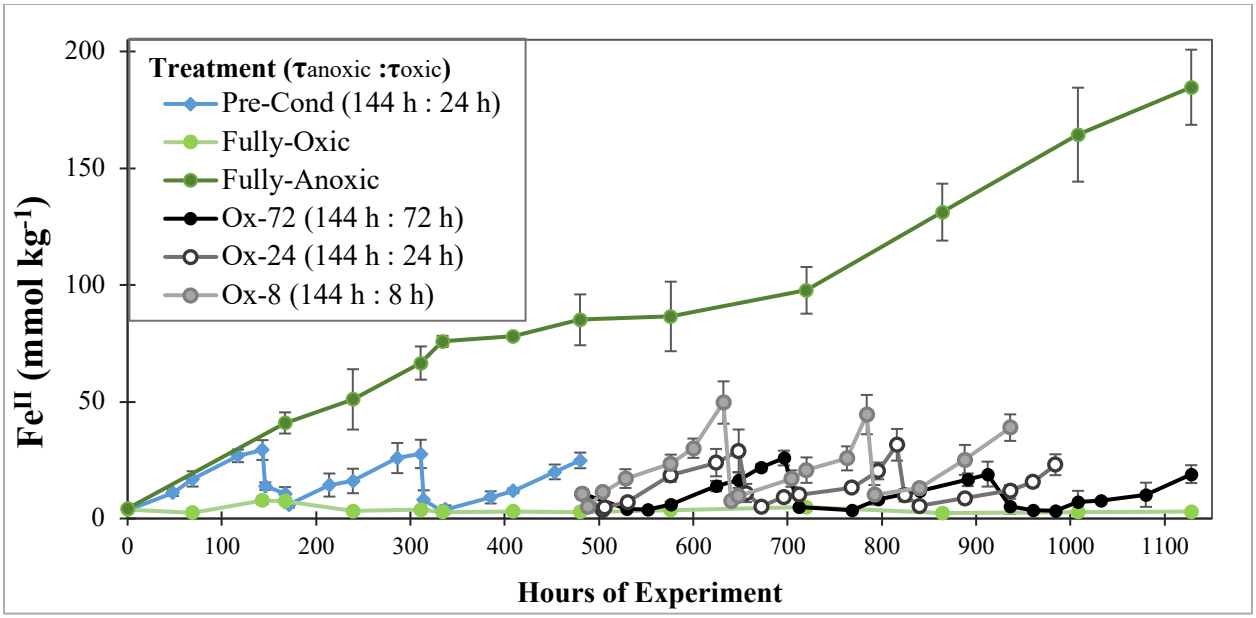

Figure S7. Fe^{II} dynamics (mean ± 1 standard deviation) for all treatments together including fully-oxic and fully-anoxic controls. In the fully-anoxic treatment (non-fluctuating), Fe^{II} concentrations increased continuously and peaked at 185 ± 16 mmol kg^{-1} at the end (equal to approximately half the soil's SRO-Fe^{III} content of 439 ± 7 mmol kg^{-1}.

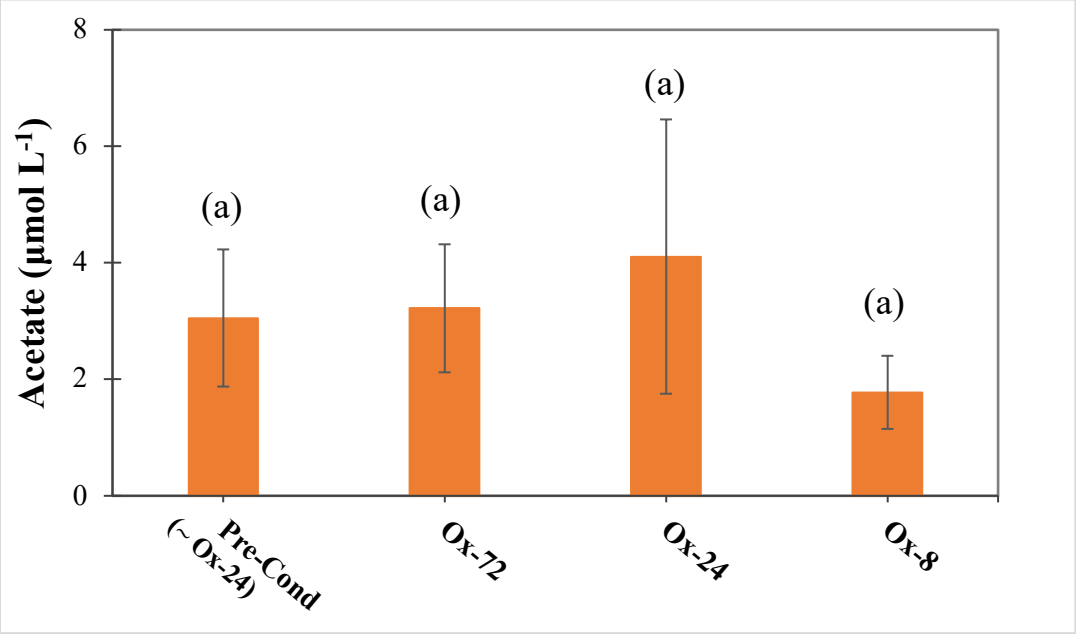

Figure S8. Acetate (µmol L^{-1}) in the aqueous phase of the reactors, sampled in the last (third) oxidation event for the treatments (Ox-72, Ox-24, and Ox-8) and for the pre-conditioning. Analyses performed in NMR for liquid samples. Different lowercase letters in parentheses indicate significant differences at the 5% probability level (ANOVA with Tukey HSD test) for each metabolite. The error bars indicate a ± 1 standard deviation.

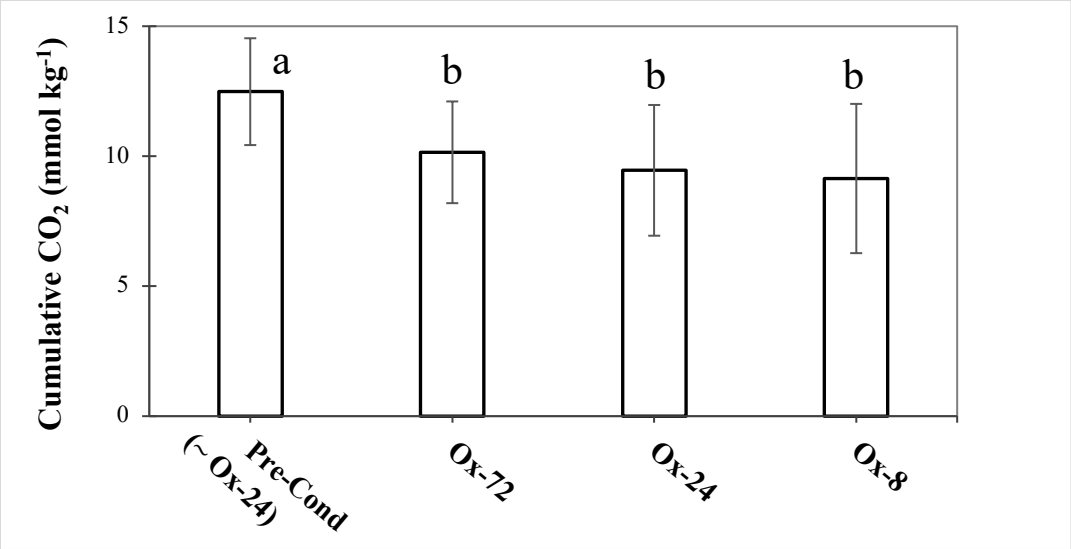

Figure S9. Cumulative CO_2 during τ_{anoxic} for each treatment. Lowercase letters in parentheses (a and b) indicate significant differences at the 5% probability level. The error bars indicate a ± 1 standard deviation.

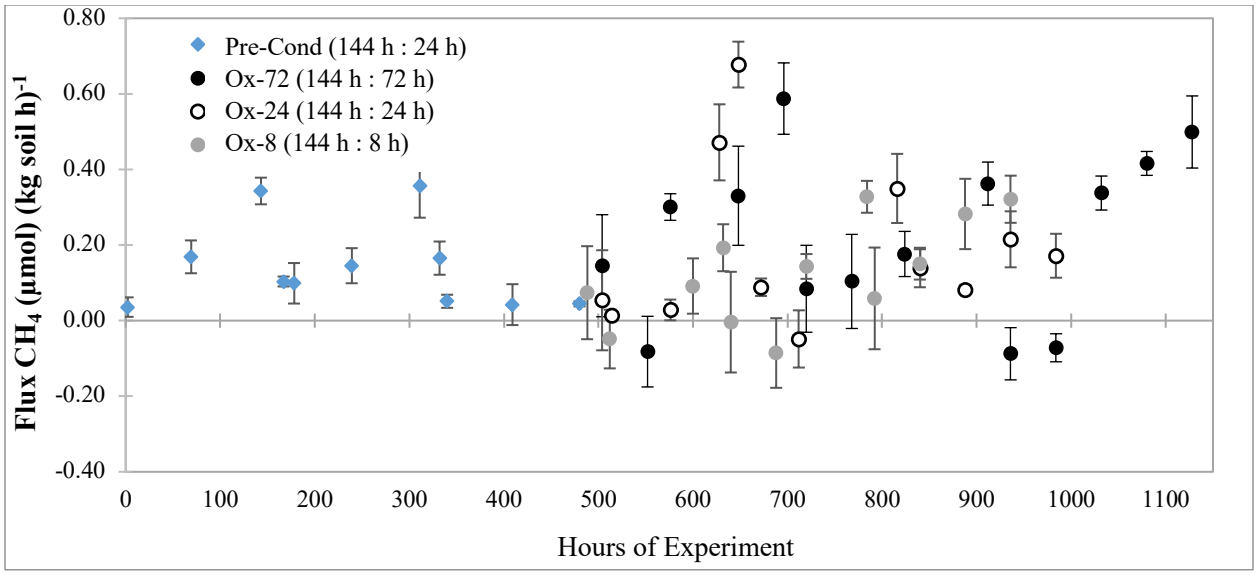
Pre-Cond (144 h : 24 h)
Ox-72 (144 h : 72 h)
Ox-24 (144 h : 24 h)
Ox-8 (144 h : 8 h)
Flux CH_4 (µmol) (kg soil h)$^{-1}$
0.80
0.60
0.40
0.20
0.00
-0.20
-0.40
0
100
200
300
400
500
600
700
800
900
1000
1100
Hours of Experiment

(a)

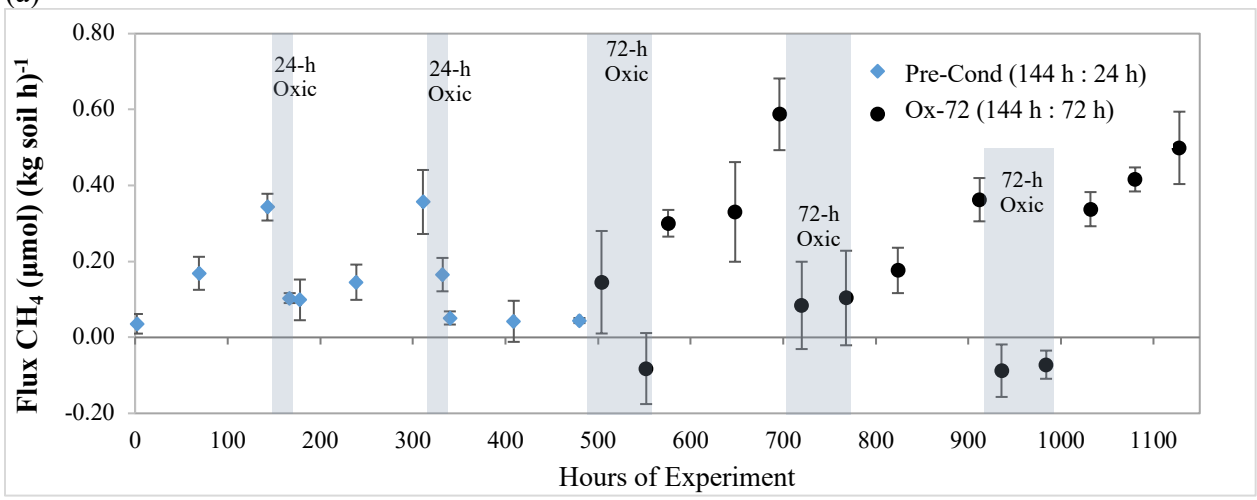
24-h Oxic
24-h Oxic
72-h Oxic
72-h Oxic
72-h Oxic
Pre-Cond (144 h : 24 h)
Ox-72 (144 h : 72 h)
Flux CH_4 (µmol) (kg soil h)$^{-1}$
0.80
0.60
0.40
0.20
0.00
-0.20
0
100
200
300
400
500
600
700
800
900
1000
1100
Hours of Experiment

(b)

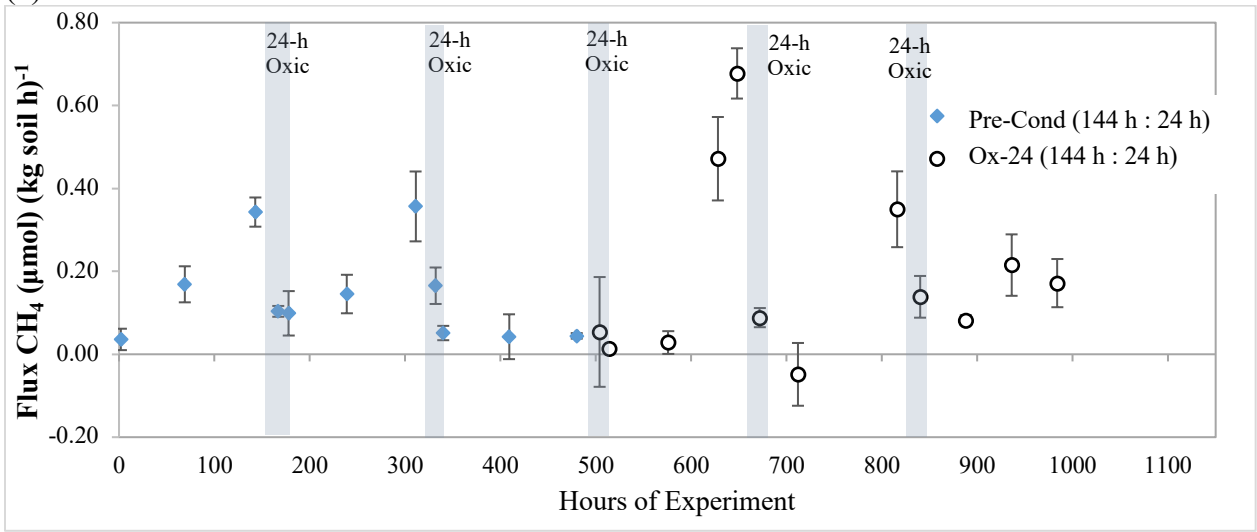
24-h Oxic
24-h Oxic
24-h Oxic
24-h Oxic
24-h Oxic
Pre-Cond (144 h : 24 h)
Ox-24 (144 h : 24 h)
Flux CH_4 (µmol) (kg soil h)$^{-1}$
0.80
0.60
0.40
0.20
0.00
-0.20
0
100
200
300
400
500
600
700
800
900
1000
1100
Hours of Experiment

(c)

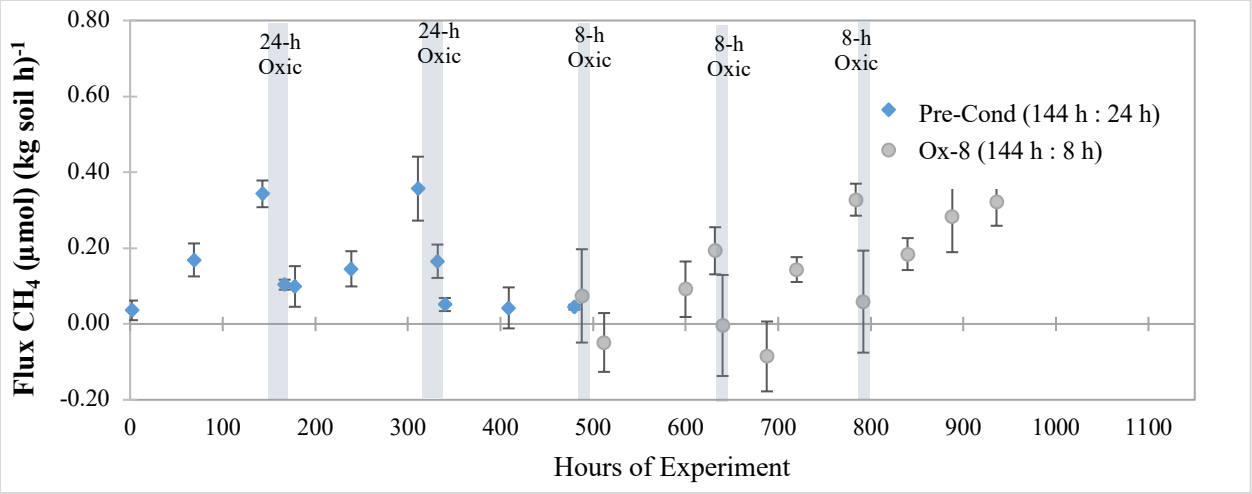

(d)

Figure S10. Instantaneous CH_4 flux for all treatments together (a) and over the different treatments (b) to (d). The error bars indicate a ± 1 standard deviation.

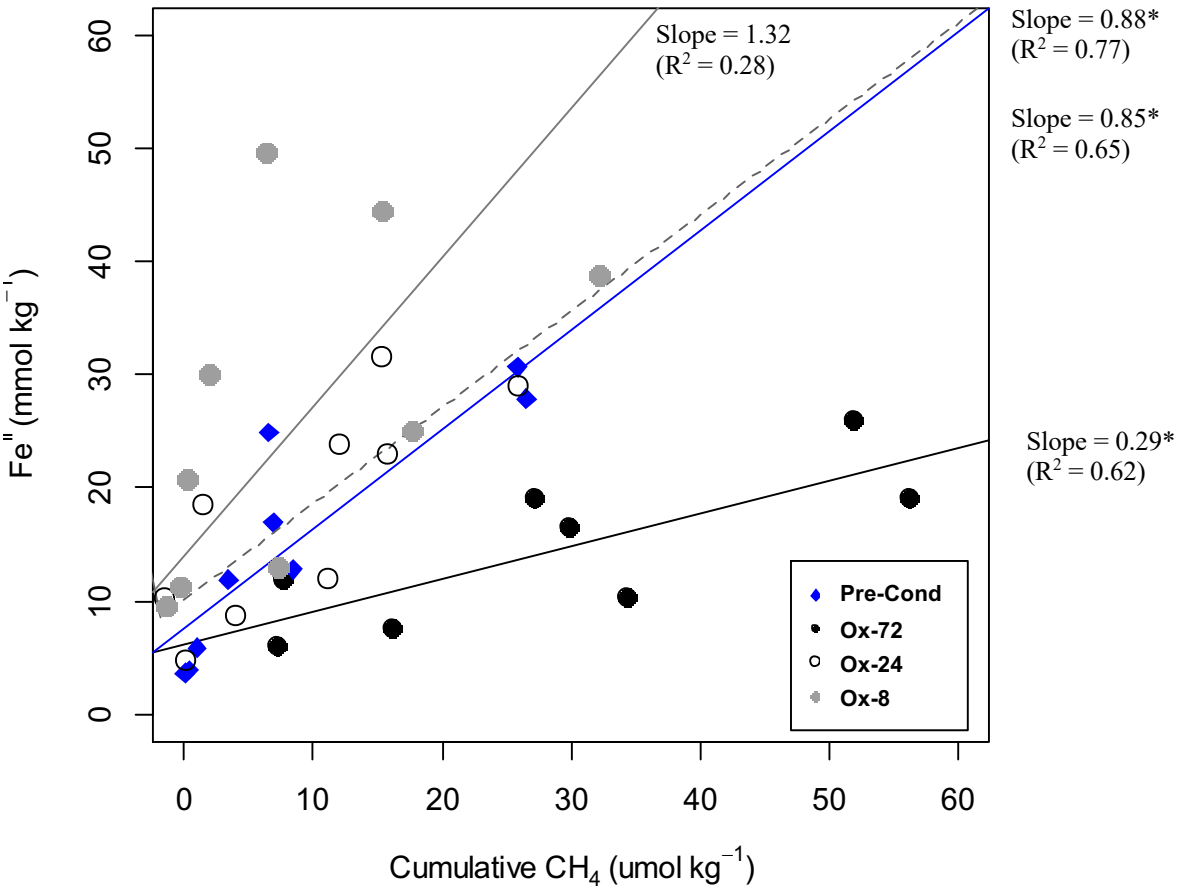

Figure S11. Linear regressions for Fe^{II} concentrations vs cumulative CH_4, under anoxic conditions only, for all treatments. Asterisks represents slopes that are significant at 5% probably for the linear models.

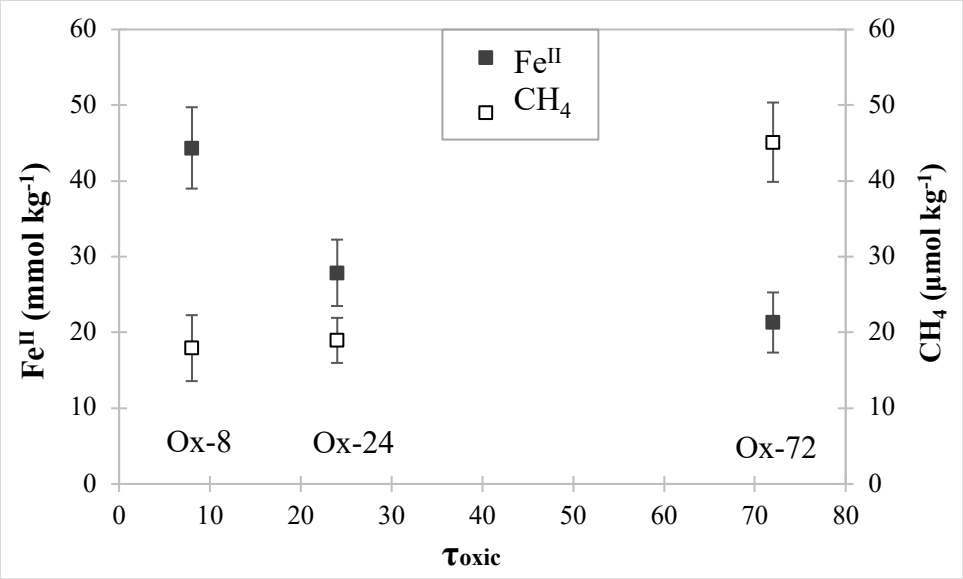

Figure S12. Soil Fe^{II} concentrations and cumulative CH_4 during anoxic conditions, comparing different previous exposed τ_{oxic} of 8, 24, and 72 h treatments.

Table S1. Total elemental analysis for initial native soil sample (no treatments or chemicals added). Soils from Bisley watershed, Puerto Rico.

Fe	Al	Si	Ca	Mg	Na	K	Ti	Mn	P
---------- mmol kg^{-1} --------			---------- % ----------						
943	2501	13636	1.54	0.65	1.00	0.43	0.39	0.14	0.035

Short-range-ordered Iron phases by citrate-ascorbate extration[16] ($SRO\text{-}Fe^{III}$) = 439 ± 7 mmol kg^{-1}.

Table S2. Dissolved oxygen (DO) concentrations exposed to anoxic conditions, from soil slurries previously exposed to oxic conditions. Zero time is still under oxic condition, measurements taken right before placing inside the anoxic chamber. Soils from Bisley watershed, Puerto Rico.

Time exposed to anoxic conditions	**Dissolved Oxygen (DO)**
Hours	$\mu g\ L^{-1}$
0	9800 ± 100
0.05	2967 ± 208
0.1	1068 ± 46
2	241 ± 13
5	119 ± 9

Table S3. Mössbauer spectral parameters for the soil at the beginning of the redox oscillation experiment (initial soil). The spectra are presented in Figure S3.

Sample	Phase	Area	$\overline{CS}$ or δ_0	$\bar{\epsilon}$	P	Δ or H	σ	$\overline{QS}$ or $\overline{H}$	χ^2_ν
Inital Soil 5K	QSD site 1	9.69(44)	0.4648(84)	n/a	100*	0.650(13)	0.195(20)	0.65	2.08
	QSD site 2	1.78(36)	1.230(28)	n/a	100*	2.903(56)	0.11(12)	2.9	
	QSD site 3	5.19(49)	0.923(15)	n/a	100*	0.983(27)	0.252(47)	0.98	
	HFD site 1	61.3(14)	0.4798(29)	-0.0970(29)	42.7068*	49.572(38)	0.923(65)	48.35	
					57.3(24)	47.45(16)	3.67(12)		
	HFD site 2	20.2(12)	0.48*	0*	100*	0*	20*	15.96	
(BG = 4.4 MC/ch)	HFD site 3	1.8(15)	1.47*	1*	100*	0*	11.5*	9.18	

BG = background level, in mega-counts per channel (MC/ch).

$Phase$ = assigned spectral component, as described in the text.

$\overline{CS}$ **or** δ_0 = the center shift of a Gaussian component in the quadrupole splitting distribution (QSD) of the hyperfine field distribution (HFD) of a given spectral component, given in mm s^{-1} .

$\overline{QS}$ = the center shift of a Gaussian component in the quadrupole splitting distribution (QSD) of the hyperfine field distribution (HFD) of a given spectral component, given in mm s^{-1} .

σ = the Gaussian standard deviation width of a given Gaussian component of a given QSD or HFD.

P = the weight factor (%) for a given Gaussian component in a given QSD or HFD.

H and $\overline{H}$ = the average magnitude of the hyperfine field (expressed as an excited state Zeeman splitting, in Torr (T), in a given HFD of a given sextet spectral component, or all components, respectively.

Δ = the average magnitude of the quadrupole splitting in a given QSD of a given doublet spectral component, given in mm s^{-1}.

$\bar{\epsilon}$ = the average magnitude of the slave distribution of quadrupole shifts (ϵ) associated to a given HFD of a given sextet spectral component, given in mm s^{-1}.

χ^2_ν = the reduced chi-squared value for the fit: chi-squared (χ^2) divided by the number of degrees of freedom (ν). It has an ideal value of 1 for a correct model.

All fits performed using the Voigt-based fitting method of Rancourt and Ping (1991) with the Recoil^{TM} software.

All fitting and calculated parameters are as defined in by Rancourt and Ping (1991).

All $\delta - 1$ couplings between CS and H (or DELTA) were taken to be zero.

All line-1 to line-2 area ratios in all (distributed) elemental doublets were taken to be 1.

All line-2/line-3 and line-1/line-3 area ratios in all (distributed and symmetric) elemental sextets were taken to be 2 and 3, respectively.

All $\epsilon - 1$ couplings between epsilon and H (in a HFD) are taken to be 0.

All Lorentzian half widths at half maximum (HWHM) are set at 0.1425 mm s^{-1} as measured on Fe foil standards on the instrument.

All center shifts ($\overline{CS}$ or δ_0) are given with respect to the CS of metallic Fe at 295K.

Table S4. Mössbauer spectral parameters for soils collected at the end of the last (third) oxic interval, for the redox oscillation treatment **Ox-72** (oxygenation for 72 h). The spectra are presented in Figure S4.

Sample	Phase	Area	$\overline{CS}$ or δ_0	$\overline{\epsilon}$	P	Δ or H	σ	$\overline{QS}$ or $\overline{H}$	χ^2_ν
Ox-8 50K	QSD site 1	21.04(98)	0.3573(91)	n/a	100*	0.882(15)	0.261(22)	0.88	1.11
	QSD site 2	12.31(71)	1.074(11)	n/a	100*	3.183(23)	0.206(33)	3.18	
	QSD site 3	11.21(72)	0.8449(79)	n/a	100*	1.252(16)	0.053(57)	1.25	
	HFD site 1	39.8(14)	0.476(11)	-0.132(11)	47.6378*	48.66(11)	1.03(18)	46.17	
					52.4(62)	43.90(94)	5.10(54)		
(BG = 1.2 MC/ch)	HFD site 2	15.7(20)	0.48*	0*	100*	0*	20*	15.96	
Ox-8 35K	QSD site 1	17.29(67)	0.3404(68)	n/a	100*	0.919(11)	0.222(17)	0.92	1.17
	QSD site 2	12.79(49)	1.0696(65)	n/a	100*	3.219(13)	0.159(21)	3.22	
	QSD site 3	13.13(58)	0.8311(60)	n/a	100*	1.255(12)	0.147(21)	1.25	
	HFD site 1	43.3(12)	0.4790(64)	-0.1175(64)	54.4397*	48.890(66)	1.14(13)	46.85	
					45.6(76)	44.41(81)	3.90(54)		
(BG = 1.3 MC/ch)	HFD site 2	13.5(15)	0.48*	0*	100*	0*	20*	15.96	
Ox-8 25K	QSD site 1	14.95(66)	0.3369(78)	n/a	100*	0.916(14)	0.187(22)	0.92	1.02
	QSD site 2	12.82(54)	1.0746(80)	n/a	100*	3.195(16)	0.193(24)	3.19	
	QSD site 3	13.18(60)	0.8264(71)	n/a	100*	1.277(14)	0.161(24)	1.28	
	HFD site 1	46.4(11)	0.4780(60)	-0.1189(60)	52.3824*	49.202(66)	0.94(13)	47.52	
					47.6(69)	45.68(63)	3.33(36)		
(BG = 1 MC/ch)	HFD site 2	12.7(15)	0.48*	0*	100*	0*	20*	15.96	
Ox-8 13K	QSD site 1	14.08(59)	0.3342(79)	n/a	100*	0.920(14)	0.206(21)	0.92	1.33
	QSD site 2	12.10(47)	1.0739(73)	n/a	100*	3.193(15)	0.187(23)	3.19	
	QSD site 3	12.44(52)	0.8318(63)	n/a	100*	1.272(12)	0.139(22)	1.27	
	HFD site 1	51.6(10)	0.4770(46)	-0.1074(46)	57.0762*	49.328(54)	1.02(10)	47.9	
					42.9(60)	46.00(58)	3.35(31)		
(BG = 1.4 MC/ch)	HFD site 2	9.8(14)	0.48*	0*	100*	0*	20*	15.96	
Ox-8 5K	QSD site 1	14.8(18)	0.404(19)	n/a	100*	0.754(30)	0.272(48)	0.75	0.63
	QSD site 2	9.3(14)	1.206(17)	n/a	100*	2.912(35)	0.185(64)	2.91	
	QSD site 3	5.6(12)	0.872(24)	n/a	100*	1.205(51)	0.06(14)	1.21	
	HFD site 1	45.0(42)	0.4737(84)	-0.1122(84)	58.36*	49.534(97)	0.81(18)	48.38	
					42(10)	46.76(96)	3.14(53)		
	HFD site 2	17.0(54)	0.48*	0*	100*	0*	20*	15.96	
(BG = 3.3 MC/ch)	HFD site 3	8.3(57)	1.24(25)	1*	100*	0*	11.5(68)	9.16	

BG = background level, in mega-counts per channel (MC/ch).

$Phase$ = assigned spectral component, as described in the text.

$\overline{CS}$ **or** δ_0 = the center shift of a Gaussian component in the quadrupole splitting distribution (QSD) of the hyperfine field distribution (HFD) of a given spectral component, given in mm s^{-1} .

$\overline{QS}$ = the center shift of a Gaussian component in the quadrupole splitting distribution (QSD) of the hyperfine field distribution (HFD) of a given spectral component, given in mm s^{-1} .

σ = the Gaussian standard deviation width of a given Gaussian component of a given QSD or HFD.

P = the weight factor (%) for a given Gaussian component in a given QSD or HFD.

H and $\overline{H}$ = the average magnitude of the hyperfine field (expressed as an excited state Zeeman splitting, in Torr (T), in a given HFD of a given sextet spectral component, or all components, respectively.

Δ = the average magnitude of the quadrupole splitting in a given QSD of a given doublet spectral component, given in mm s^{-1}.

$\overline{\epsilon}$ = the average magnitude of the slave distribution of quadrupole shifts (ϵ) associated to a given HFD of a given sextet spectral component, given in mm s^{-1}.

χ^2_ν = the reduced chi-squared value for the fit: chi-squared (χ^2) divided by the number of degrees of freedom (ν). It has an ideal value of 1 for a correct model.

All fits performed using the Voigt-based fitting method of Rancourt and Ping (1991) with the Recoil^{TM} software.

All fitting and calculated parameters are as defined in by Rancourt and Ping (1991).

All $\delta - 1$ couplings between CS and H (or DELTA) were taken to be zero.

All line-1 to line-2 area ratios in all (distributed) elemental doublets were taken to be 1.

All line-2/line-3 and line-1/line-3 area ratios in all (distributed and symmetric) elemental sextets were taken to be 2 and 3, respectively.

All $\epsilon - 1$ couplings between epsilon and H (in a HFD) are taken to be 0.

All Lorentzian half widths at half maximum (HWHM) are set at 0.1425 mm s^{-1} as measured on Fe foil standards on the instrument.

All center shifts ($\overline{CS}$ or δ_0) are given with respect to the CS of metallic Fe at 295K.

Table S5. Mössbauer spectral parameters for soils collected at the end of the last (third) oxic interval, for the redox oscillation treatment **Ox-24** (oxygenation for 24 h). The spectra are presented in Figure S5.

Sample	Phase	Area	$\overline{CS}$ or δ_0	$\bar{\epsilon}$	P	Δ or H	σ	$\overline{QS}$ or $\overline{H}$	χ^2_ν
Ox-24 50K	QSD site 1	29.8(15)	0.3817(97)	n/a	100*	0.833(16)	0.290(23)	0.83	0.67
	QSD site 2	15.7(10)	1.098(12)	n/a	100*	3.184(24)	0.204(35)	3.18	
	QSD site 3	11.91(98)	0.854(10)	n/a	100*	1.243(21)	0.053(74)	1.24	
	HFD site 1	30.7(17)	0.481(14)	-0.130(14)	68.0536*	48.70(13)	0.99(28)	47.13	
					32(19)	43.8(28)	3.5(21)		
(BG = 5.5 MC/ch)	HFD site 2	11.9(27)	0.48*	0*	100*	0*	20*	15.96	
Ox-24 35K	QSD site 1	24.1(19)	0.372(15)	n/a	100*	0.862(24)	0.263(37)	0.86	0.66
	QSD site 2	16.1(15)	1.114(18)	n/a	100*	3.146(37)	0.257(50)	3.15	
	QSD site 3	13.2(15)	0.852(16)	n/a	100*	1.249(33)	0.142(57)	1.25	
	HFD site 1	36.7(24)	0.491(18)	-0.113(18)	72.2531*	48.82(25)	1.27(34)	47.36	
					28(25)	43.5(37)	3.1(29)		
(BG = 2.9 MC/ch)	HFD site 2	9.8(39)	0.48*	0*	100*	0*	20*	15.96	
Ox-24 25K	QSD site 1	21.4(14)	0.354(12)	n/a	100*	0.867(21)	0.207(31)	0.87	0.66
	QSD site 2	14.4(11)	1.095(16)	n/a	100*	3.170(32)	0.221(45)	3.17	
	QSD site 3	12.5(12)	0.850(13)	n/a	100*	1.247(25)	0.098(57)	1.25	
	HFD site 1	38.5(20)	0.490(13)	-0.107(13)	49.1033*	49.29(14)	0.70(28)	47.78	
					51(13)	46.3(11)	3.07(63)		
(BG = 3.9 MC/ch)	HFD site 2	13.3(30)	0.49*	0*	100*	0*	20*	15.96	
Ox-24 13K	QSD site 1	17.4(16)	0.370(18)	n/a	100*	0.850(30)	0.226(47)	0.85	0.66
	QSD site 2	15.2(14)	1.133(20)	n/a	100*	3.081(41)	0.282(55)	3.08	
	QSD site 3	12.8(14)	0.845(16)	n/a	100*	1.243(32)	0.129(59)	1.24	
	HFD site 1	43.1(24)	0.470(13)	-0.133(13)	31.5236*	49.58(15)	0.25(46)	48.58	
					68.5(86)	48.12(45)	2.89(41)		
(BG = 2.8 MC/ch)	HFD site 2	11.6(36)	0.48*	0*	100*	0*	20*	15.96	
Ox-24 5K	QSD site 1	9.41(78)	0.397(13)	n/a	100*	0.822(31)	0.252(45)	0.82	0.94
	QSD site 2	7.99(65)	1.226(12)	n/a	100*	2.902(24)	0.205(39)	2.9	
	QSD site 3	5.64(57)	0.846(14)	n/a	100*	1.217(26)	0.108(52)	1.22	
	HFD site 1	46.5(20)	0.4766(41)	-0.1069(41)	52.6774*	49.522(53)	0.756(97)	48.51	
					47.3(51)	47.38(35)	2.88(20)		
	HFD site 2	22.4(22)	0.48*	0*	100*	0*	20*	15.96	
(BG = 1.9 MC/ch)	HFD site 3	8.0(27)	1.56(19)	1*	100*	0*	11.3(33)	9.04	

BG = background level, in mega-counts per channel (MC/ch).

$Phase$ = assigned spectral component, as described in the text.

$\overline{CS}$ **or** δ_0 = the center shift of a Gaussian component in the quadrupole splitting distribution (QSD) of the hyperfine field distribution (HFD) of a given spectral component, given in mm s^{-1} .

$\overline{QS}$ = the center shift of a Gaussian component in the quadrupole splitting distribution (QSD) of the hyperfine field distribution (HFD) of a given spectral component, given in mm s^{-1} .

σ = the Gaussian standard deviation width of a given Gaussian component of a given QSD or HFD.

P = the weight factor (%) for a given Gaussian component in a given QSD or HFD.

H and $\overline{H}$ = the average magnitude of the hyperfine field (expressed as an excited state Zeeman splitting, in Torr (T), in a given HFD of a given sextet spectral component, or all components, respectively.

Δ = the average magnitude of the quadrupole splitting in a given QSD of a given doublet spectral component, given in mm s^{-1}.

$\bar{\epsilon}$ = the average magnitude of the slave distribution of quadrupole shifts (ϵ) associated to a given HFD of a given sextet spectral component, given in mm s^{-1}.

χ^2_ν = the reduced chi-squared value for the fit: chi-squared (χ^2) divided by the number of degrees of freedom (ν). It has an ideal value of 1 for a correct model.

All fits performed using the Voigt-based fitting method of Rancourt and Ping (1991) with the Recoil^{TM} software.

All fitting and calculated parameters are as defined in by Rancourt and Ping (1991).

All $\delta - 1$ couplings between CS and H (or DELTA) were taken to be zero.

All line-1 to line-2 area ratios in all (distributed) elemental doublets were taken to be 1.

All line-2/line-3 and line-1/line-3 area ratios in all (distributed and symmetric) elemental sextets were taken to be 2 and 3, respectively.

All $\epsilon - 1$ couplings between epsilon and H (in a HFD) are taken to be 0.

All Lorentzian half widths at half maximum (HWHM) are set at 0.1425 mm s^{-1} as measured on Fe foil standards on the instrument.

All center shifts ($\overline{CS}$ or δ_0) are given with respect to the CS of metallic Fe at 295K.

Table S6. Mössbauer spectral parameters for soils collected at the end of the last (third) oxic interval, for the redox oscillation treatment **Ox-8** (oxygenation for 8 h). The spectra are presented in Figure S6.

Sample	Phase	Area	$\overline{CS}$ or δ_0	$\bar{\epsilon}$	P	Δ or H	σ	$\overline{QS}$ or $\overline{H}$	χ^2_ν
Ox-72 50K	QSD site 1	25.6(19)	0.380(13)	n/a	100*	0.838(21)	0.281(31)	0.84	0.55
	QSD site 2	13.7(13)	1.101(20)	n/a	100*	3.152(39)	0.258(51)	3.15	
	QSD site 3	10.8(12)	0.858(13)	n/a	100*	1.253(27)	0.05(11)	1.25	
	HFD site 1	36.1(25)	0.483(18)	-0.110(18)	61.5807*	48.55(16)	1.24(28)	45.69	
					38(13)	41.1(31)	6.1(23)		
(BG = 4.8 MC/ch)	HFD site 2	13.7(37)	0.48*	0*	100*	0*	20*	15.96	
Ox-72 35K	QSD site 1	21.0(19)	0.359(17)	n/a	100*	0.845(27)	0.251(41)	0.84	0.62
	QSD site 2	14.1(15)	1.098(21)	n/a	100*	3.177(43)	0.254(56)	3.18	
	QSD site 3	11.8(15)	0.844(18)	n/a	100*	1.238(36)	0.134(63)	1.24	
	HFD site 1	43.7(29)	0.487(19)	-0.123(19)	53.6259*	48.85(18)	1.24(28)	46.1	
					46(10)	42.9(23)	6.2(13)		
(BG = 3.7 MC/ch)	HFD site 2	9.4(43)	0.48*	0*	100*	0*	20*	15.96	
Ox-72 25K	QSD site 1	22.3(17)	0.361(15)	n/a	100*	0.907(25)	0.259(39)	0.91	0.66
	QSD site 2	15.3(13)	1.089(16)	n/a	100*	3.192(33)	0.209(47)	3.19	
	QSD site 3	14.0(14)	0.839(16)	n/a	100*	1.273(33)	0.172(51)	1.27	
	HFD site 1	41.7(24)	0.485(14)	-0.120(14)	62.8113*	49.24(16)	0.99(38)	47.89	
					37(31)	45.6(29)	2.7(18)		
(BG = 5 MC/ch)	HFD site 2	6.6(37)	0.48*	0*	100*	0*	20*	15.96	
Ox-72 13K	QSD site 1	18.2(16)	0.315(19)	n/a	100*	0.885(31)	0.247(46)	0.88	0.66
	QSD site 2	13.0(13)	1.077(17)	n/a	100*	3.219(35)	0.175(56)	3.22	
	QSD site 3	14.0(14)	0.831(16)	n/a	100*	1.293(33)	0.173(53)	1.29	
	HFD site 1	46.9(24)	0.471(11)	-0.106(11)	51.591*	49.63(14)	0.66(30)	48.41	
					48(19)	47.1(12)	2.40(63)		
(BG = 4.4 MC/ch)	HFD site 2	7.8(36)	0.48*	0*	100*	0*	20*	15.96	
Ox-72 5K	QSD site 1	14.0(12)	0.424(13)	n/a	100*	0.745(26)	0.288(45)	0.75	0.71
	QSD site 2	9.18(92)	1.229(13)	n/a	100*	2.894(26)	0.206(44)	2.89	
	QSD site 3	4.62(82)	0.849(26)	n/a	100*	1.159(58)	0.137(83)	1.16	
	HFD site 1	48.3(28)	0.4758(54)	-0.1118(53)	55.7568*	49.514(66)	0.84(12)	48.51	
					44.2(60)	47.25(50)	3.21(30)		
	HFD site 2	17.7(32)	0.48*	0*	100*	0*	20*	15.96	
(BG = 3 MC/ch)	HFD site 3	6.1(37)	1.47(29)	1*	100*	0*	11.5(60)	9.16	

BG = background level, in mega-counts per channel (MC/ch).

$Phase$ = assigned spectral component, as described in the text.

$\overline{CS}$ **or** δ_0 = the center shift of a Gaussian component in the quadrupole splitting distribution (QSD) of the hyperfine field distribution (HFD) of a given spectral component, given in mm s^{-1} .

$\overline{QS}$ = the center shift of a Gaussian component in the quadrupole splitting distribution (QSD) of the hyperfine field distribution (HFD) of a given spectral component, given in mm s^{-1} .

σ = the Gaussian standard deviation width of a given Gaussian component of a given QSD or HFD.

P = the weight factor (%) for a given Gaussian component in a given QSD or HFD.

H and $\overline{H}$ = the average magnitude of the hyperfine field (expressed as an excited state Zeeman splitting, in Torr (T), in a given HFD of a given sextet spectral component, or all components, respectively.

Δ = the average magnitude of the quadrupole splitting in a given QSD of a given doublet spectral component, given in mm s^{-1}.

$\bar{\epsilon}$ = the average magnitude of the slave distribution of quadrupole shifts (ϵ) associated to a given HFD of a given sextet spectral component, given in mm s^{-1}.

χ^2_ν = the reduced chi-squared value for the fit: chi-squared (χ^2) divided by the number of degrees of freedom (ν). It has an ideal value of 1 for a correct model.

All fits performed using the Voigt-based fitting method of Rancourt and Ping (1991) with the Recoil^{TM} software.

All fitting and calculated parameters are as defined in by Rancourt and Ping (1991).

All $\delta - 1$ couplings between CS and H (or DELTA) were taken to be zero.

All line-1 to line-2 area ratios in all (distributed) elemental doublets were taken to be 1.

All line-2/line-3 and line-1/line-3 area ratios in all (distributed and symmetric) elemental sextets were taken to be 2 and 3, respectively.

All $\epsilon - 1$ couplings between epsilon and H (in a HFD) are taken to be 0.

All Lorentzian half widths at half maximum (HWHM) are set at 0.1425 mm s^{-1} as measured on Fe foil standards on the instrument.

All center shifts ($\overline{CS}$ or δ_0) are given with respect to the CS of metallic Fe at 295K.

Table S7. Linear regression of Fe^{II} concentration (mmol kg^{-1}) and cumulative CH_4 (μmol kg^{-1}) with slopes and R^2 for each treatment comparison. See Figure S9.

Treatment	Linear regression (Fe^{II} concentration vs Cumulative CH_4)	
	Slope	**R^2**
All treatments	0.33*	0.18
Pre-conditioning	0.88*	0.77
Ox-72	0.29*	0.62
Ox-24	0.85*	0.65
Ox-8	1.32	0.28

*significant relationship between variables at the 5% probability level.

Supplementary References

1. Chen, C.; Hall, S. J.; Coward, E.; Thompson, A., Iron-mediated organic matter decomposition in humid soils can counteract protection. *Nature Communications* **2020,** *11*, (1), 2255.
2. Rancourt, D. G.; Ping, J. Y., Voigt-based methods for arbitrary-shape static hyperfine parameter distributions in Mössbauer spectroscopy. *Nuclear Instruments and Methods in Physics Research Section B: Beam Interactions with Materials and Atoms* **1991,** *58*, (1), 85-97.
3. Caporaso, J. G.; Lauber, C. L.; Walters, W. A.; Berg-Lyons, D.; Huntley, J.; Fierer, N.; Owens, S. M.; Betley, J.; Fraser, L.; Bauer, M.; Gormley, N.; Gilbert, J. A.; Smith, G.; Knight, R., Ultra-high-throughput microbial community analysis on the Illumina HiSeq and MiSeq platforms. *The ISME Journal* **2012,** *6*, (8), 1621-1624.
4. Caporaso, J. G.; Kuczynski, J.; Stombaugh, J.; Bittinger, K.; Bushman, F. D.; Costello, E. K.; Fierer, N.; Peña, A. G.; Goodrich, J. K.; Gordon, J. I.; Huttley, G. A.; Kelley, S. T.; Knights, D.; Koenig, J. E.; Ley, R. E.; Lozupone, C. A.; McDonald, D.; Muegge, B. D.; Pirrung, M.; Reeder, J.; Sevinsky, J. R.; Turnbaugh, P. J.; Walters, W. A.; Widmann, J.; Yatsunenko, T.; Zaneveld, J.; Knight, R., QIIME allows analysis of high-throughput community sequencing data. *Nature Methods* **2010,** *7*, (5), 335-336.
5. Callahan, B. J.; McMurdie, P. J.; Rosen, M. J.; Han, A. W.; Johnson, A. J. A.; Holmes, S. P., DADA2: High-resolution sample inference from Illumina amplicon data. *Nature Methods* **2016,** *13*, (7), 581-583.
6. Yilmaz, P.; Parfrey, L. W.; Yarza, P.; Gerken, J.; Pruesse, E.; Quast, C.; Schweer, T.; Peplies, J.; Ludwig, W.; Glöckner, F. O., The SILVA and "All-species Living Tree Project (LTP)" taxonomic frameworks. *Nucleic Acids Research* **2013,** *42*, (D1), D643-D648.
7. Edgar, R. C., MUSCLE: multiple sequence alignment with high accuracy and high throughput. *Nucleic Acids Research* **2004,** *32*, (5), 1792-1797.
8. Price, M. N.; Dehal, P. S.; Arkin, A. P., FastTree 2 – Approximately Maximum-Likelihood Trees for Large Alignments. *PLOS ONE* **2010,** *5*, (3), e9490.
9. McMurdie, P. J.; Holmes, S., phyloseq: An R Package for Reproducible Interactive Analysis and Graphics of Microbiome Census Data. *PLOS ONE* **2013,** *8*, (4), e61217.
10. Team, R. C., R: A language and environment for statistical computing. In Vienna, Austria: 2013.
11. Love, M. I.; Huber, W.; Anders, S., Moderated estimation of fold change and dispersion for RNA-seq data with DESeq2. *Genome Biology* **2014,** *15*, (12), 550.
12. Wickham, H. In *Data manipulation with dplyr*, R user conference, 2014; 2014.
13. Oksanen, J.; Blanchet, F. G.; Kindt, R.; Legendre, P.; Minchin, P. R.; O'hara, R.; Simpson, G. L.; Solymos, P.; Stevens, M. H. H.; Wagner, H., Package 'vegan'. *Community ecology package, version* **2013,** *2*, (9), 1-295.
14. Wickham, H., *ggplot2: elegant graphics for data analysis*. springer: 2016.
15. Barcellos, D.; Cyle, K. T.; Thompson, A., Faster redox fluctuations can lead to higher iron reduction rates in humid forest soils. *Biogeochemistry* **2018,** *137*, (3), 367-378.
16. Reyes, I.; Torrent, J., Citrate-ascorbate as a highly selective extractant for poorly crystalline iron oxides. *Soil Science Society of America Journal* **1997,** *61*, (6), 1647-1654.